



universität
wien

MASTERARBEIT

Titel der Masterarbeit

Accurate high-resolution Raman spectroscopy on carbon
nanotube forests

Verfasser

Gerald Pühringer, BSc

angestrebter akademischer Grad

Master of Science (MSc)

Wien, 2014

Studienkennzahl lt. Studienblatt:

A 066 876

Studienrichtung lt. Studienblatt:

Masterstudium Physik

Betreuer:

Univ.-Prof. Mag. Dr. Thomas Pichler

Zusammenfassung

Raman Spektroskopie gehört zu den wichtigsten Mitteln zur Untersuchung der atomaren Strukturen und elektronischen Eigenschaften mit einer großen Bandbreite an möglichen Anwendungen, insbesondere an modernen Nanomaterialien wie Graphen oder Kohlenstoff-Nanoröhren. Ein zentraler Punkt der Methode ist daher die Shift-Position der Raman Features und die Laser-Anregungsenergien mit ausreichender Präzision zu kennen. In dieser Arbeit wird ein einfaches Verfahren zur Kalibrierung der Shift-Skala eines Spektrums mit optimierter und zuverlässiger Genauigkeit präsentiert und das maximale Auflösungsvermögen des beliebten *DilorXY* Raman-Spektrometers untersucht. Unterschiedliche Proben von CVD-gewachsenen Nanoröhren wurden verglichen, charakterisiert und verschiedene Dotierungs-, bzw. Van der Waals Wechselwirkungseffekte auf der Nanoskala gefunden. Diese demonstrieren wiederum die Nützlichkeit und das Potential einer verlässlichen Raman-shift Quantifizierung. Die meisten Änderungen der Raman-shift Positionen wurden im Bereich der Atmungsmode (RBM) beobachtet, aber auch Änderungen der G-, D-, und 2D-Moden sind sehr interessant und geeignet um die Vorteile einer optimal kalibrierten Shift-Skala aufzuzeigen. Die auf Quarz-Plättchen gewachsenen Nanoröhren-’Wälder’ unterscheiden sich untereinander durch Stickstoff Dotierung und Dicke (bestimmt durch deren Wachstumsdauer). Mit Hilfe der genauen Kalibrierung konnten die verschiedenen Wechselwirkungseffekte, wie beispielsweise kollektive Schwingungszustände von großen doppelwandigen Nanoröhren (DWNTs) mit unterschiedlichen Wandabständen, zuverlässig beobachtet und bewertet werden. Das Gebiet der Wechselwirkung zwischen Nanoröhren, die verschiedenen Schwingungszustände und der Einfluss von Dotierstoffen ist bis jetzt noch nicht vollständig verstanden. Daher ist eine genaue Raman-shift Skala ein wichtiges Mittel zur präzisen Charakterisierung der Schwingungsenergien und der darauf bezogenen physikalische Effekte.

Abstract

Raman Spectroscopy is one of the most important tools to characterize the atomistic structure and electronic properties for a large variety of possible samples, especially for modern carbon-based nanomaterials like graphene or carbon nanotubes. Therefore it is a central aspect to know the shift positions of the Raman features and the laser excitation energies with sufficient precision. In this work a simple method is presented to calibrate the shift-scale of a Raman spectrum after a measurement with optimized and reliable accuracy and the maximum resolution power of the popular *Dilor XY* Raman spectrometer was analysed. Different types of CVD-grown samples were compared, characterized and various nanoscale doping/Van der Waals interaction-effects were found, which could demonstrate and test the utility and potential of a reliable Raman shift positions. Most Raman-shift- sensible effects were observed in the radial breathing mode (RBM) region, but also changes of the G-Line, D-Line and 2D-Line are very interesting and suitable quantities to show the advantages of a precise shift scale. The CNT films deposited on quartz plates differed in nitrogen doping level and thickness (deposition time). With help of the accurate calibration, the different (e.g., tube-tube) interaction effects could be reliably observed and evaluated, like the collective vibrations of large-diameter DWNTs with different interwall distances. The field of tube-tube/doping interactions and vibration patterns is not completely understood yet, which makes an accurate Raman-scale an important tool for quantifying precisely vibration energies and physical effects related to them.

Contents

1	Motivation	1
2	Introduction	3
2.1	Carbon nanotubes	3
2.1.1	Geometrical structure- zone folding scheme	3
2.1.2	Electronic structure	4
2.1.3	Phonon structure	6
2.2	Raman spectroscopy	6
2.2.1	Raman process	6
2.2.2	Stokes Raman Intensity	7
2.3	Properties of Raman modes	8
2.3.1	Radial Breathing mode	8
2.3.2	G-line	8
2.3.3	D-line	9
2.3.4	2D/G'-line	9
2.4	Double-Wall carbon nanotubes	10
2.4.1	Collective oscillations of inner and outer tubes	12
2.5	Influence of Environmental effects on the radial breathing mode (RBM)	13
2.5.1	Suspended SWCNTs	13
2.5.2	Bundling effects	14
2.5.3	DWNTs	14
3	Experimental setup	17
3.1	General Raman spectrometer	17
3.2	Dilor XY 800 - Raman Spectrometer	17
3.3	Issues spectrometer position control	18
3.4	Calibration lamps	19
3.5	Lasers	20
3.5.1	Argon-Krypton gas laser	20
3.5.2	Dye-laser	20
3.6	Set of studied samples produced by no-flow CVD	20
3.7	Experimental details	21
4	Calibration	22
4.1	The calibration problem	22
4.2	Calculation of Raman shifts and spectral range	22
4.2.1	The grating equation	22

4.2.2	Rescaling of the wavenumber-axis	23
4.2.3	Linear dispersion or resolving power	23
4.2.4	Application and Implementation	24
4.3	Application on the Dilor XY Raman spectrometer (noble gas laser)	25
4.3.1	Problem of simplification in HR-mode	25
4.3.2	Difference in calibration accuracy between NR- and HR-mode	26
4.3.3	Consistency tests	26
4.3.4	Estimation of resolution power/accuracy of calibration in HR mode . . .	28
4.4	Dye-Laser measurement calibration	30
4.4.1	Application	31
4.5	Summary of chapter 4	32
5	Raman Analysis of bundling and doping effects	34
5.1	Sample thickness	34
5.1.1	Radial breathing mode	34
5.1.2	G'-line	35
5.1.3	D and G-Line region	37
5.2	Nitrogen doping effects	38
5.2.1	Radial Breathing Mode	38
5.2.2	G-band	40
5.2.3	G'-line	41
5.3	Summary of chapter 5	43
6	Detailed Raman analysis of DWNT RBM-clusters	45
6.1	Experimental results	46
6.1.1	0 % sample measurements	46
6.1.2	5 % sample measurements: N ₂ - Doping effects	53
6.2	Discussion of inner tube resonances	55
6.2.1	Splitting cluster width	55
6.2.2	Assignment to outer tubes	56
6.2.3	Intensity and linewidth	59
6.2.4	Growth process	62
6.3	Summary of chapter 6	65
7	Conclusions and future perspectives	67

List of Figures

2.1	Unrolled nanotube as graphene	3
2.2	Graphene real space, reziprocal space and cutting lines	4
2.3	Electron dispersions	4
2.4	Kataura Plot with resonance areas	5
2.5	Determination of metallicity	5
2.6	Phonon dispersions	7
2.7	Raman process	8
2.8	Double Walled vs. Single Walled nanotubes	10
2.9	Peapod vs. CVD - DWNTs	11
2.10	Two coupled oscillators	12
2.11	Simulated DWNT interaction potentials	15
3.1	Simplified general Raman Spectrometer	17
3.2	Dilor XY: High and normal resolution mode	19
3.3	All lamp line positions for $\lambda_l=400$ nm	19
4.1	Geometry for Raman scale recalculation	23
4.2	NR-HR consistency test for RBM-features	27
4.3	NR-HR consistency test: Calibration lamp lines in RBM region	28
4.4	Increase of Raman shift error with spectrometer position	28
4.5	NR-HR accuracy test with DWNT cluster	29
4.6	Confidence Interwall for Raman accuracy	30
4.7	Dye-Laser: Change in dispersion through wavelength correction	32
5.1	Sample thickness influence on RBM features	35
5.2	Sample thickness influence on G'-Line features	36
5.3	D and G band with varying sample film thickness at 568 and 488 nm	38
5.4	0 %, 3 % and 5 % RBM modes 568 nm	39
5.5	Nitrogen influence on RBM modes: 0 % and 5 % samples at 514 nm	40
5.6	Doping effects on the G-band	41
5.7	G'-Lines of 0 %, 3 % and 5 % samples: Nitrogen influence	43
6.1	0 % sample RBM-features from 465 to 568 nm	47
6.2	Deconvolution of all observed DWNT-splitting clusters	50
6.3	RBM peaks of 5 % sample from 488 to 568 nm	54
6.4	Linear fit of data from ref. [19] for outer tube assignment	57

6.5	Plot WtW-distance vs. Raman-blueshift of all clusters based on tube assignment	59
6.6	Deconvolution of cluster (10,7) in HR mode for natural FWHM	61
6.7	Growth process of cluster (9,6)	63

List of abbreviations

Abbreviation	Meaning
SW(C)NT	Single walled (carbon) nanotube
DW(C)NT	Double walled (carbon) nanotube
WtW	Wall to wall
(C)CVD	(Catalyst) Chemical vapour deposition
LA, TA, LO, TO	Longitudinal acoustic, transverse acoustic, longitudinal optical, transverse optical
sccm	standard cubic centimeters per minute
RBM	Radial breathing mode
NR, HR	Normal resolution, high resolution
FWHM	Full width at half maximum

1 Motivation

Carbon nanotubes (CNT) play a central role in the field of nanoscience and nanotechnology because of their unique mechanical and electronic properties and high potential for a wide range of applications. A challenge for the nanotechnologies is to achieve perfect control over the nanoscale related properties, not only for CNTs. Obviously, the parameters of the synthesis process have to be correlated to the resulting nanostructures. One of the most powerful tools for the characterization of carbon nanotubes is Raman spectroscopy, which is the inelastic scattering of light by any kind of matter, from molecules to crystals. The effect is highly sensitive to the vibrational and electronic properties of the scattering material, as well as to any environmental effects at the nanoscale that may change these properties. The method is non-destructive and non-invasive (like all optical techniques) and does only require very simple or no specific sample preparation.

This work mainly focuses on the vibrational properties of carbon nanotubes and changes of them due to environmental effects. To understand these properties precisely, it is frequently very useful to resolve the energies of the vibrational modes accurately. For instance, this allows to detect slight changes in vibration energies between distinct measurement parameters reliably, which directly affects the scope and the reliability of the information that can be gained from of a Raman-spectrum.

The energies of the measured vibration modes is represented by the Raman-shift scale. This scale has to be calibrated in order to gain sufficient accuracy for the vibration energies. This calibration is based on the accuracy of the known emission line-energies of various chemical elements (, e.g. Neon, Mercury, Xenon,...), which should allow exceedingly precision for the Raman-scale calibration, in theory. Unfortunately, the resolving power of a Raman spectrometer is always limited and determined by its geometrical properties. A calibration is the requirement for exploiting a specific resolving power. Therefore, a simple way to optimize the accuracy of the Raman-scale for a given resolution power and minimize the experimental effort is very useful in everyday labour-life and important to maximize the information content gained from the spectra.

The first part of this thesis presents and analyses a simple way of calculating the Raman-scale based on the geometrical properties of the Raman spectrometer. This method allows an effortless and comprehensible reproduction and correction of the Raman-scale after the measurements were performed. In certain scenarios with suboptimal circumstances (e.g., the absence of emission-lines in certain spectral windows) this can also mean an even larger improvement in reliability.

The second part analyses Raman-shift sensitive effects, which are related to environmental effects on the nanoscale, based on no-flow CVD produced nanotube-forests grown on quartz plates. The majority of these effects stem from tube-tube (Van der Waals-) interactions, but some are also related to defects or substitutional dopants. These dopants

1 Motivation

cause charged defect-sites, which may influence certain vibration patterns. Tube-tube interactions can lead to, for instance, collective bundle or multi-walled CNT vibrations, which contain vastly different vibration energies for the Radial-Breathing Mode (RBM) compared to individually oscillating nanotubes. For this reason samples with possibly distinct nanotube-array arrangements (different carbon-film thickness) and different doping levels were chosen for characterization. Some samples feature unexpected types of RBM-resonances, which could be related to DWNT vibrations. This offered a good possibility of very interesting analysis of the observed phenomena by using exclusively Raman-spectroscopy. Additionally, the study clearly demonstrates the importance of a reliable and accurate calibration for the investigation of small Raman-shift related effects.

2 Introduction

2.1 Carbon nanotubes

2.1.1 Geometrical structure- zone folding scheme

A single walled carbon nanotube can be described as a single layer graphite crystal rolled up into a seamless cylinder. The nanoscale of the circumference leads to quantum confinement, whose effects can be described via the zone-folding scheme.

The graphene layer coordinate system is oriented in such a way that the armchair direction lies along the x-Axis and the zigzag direction along the y-axis, as shown in figure 2.1. The nanotube structure is determined by the chiral vector $\mathbf{C}_h = n\mathbf{a}_1 + m\mathbf{a}_2$, where \mathbf{a}_1 and \mathbf{a}_2 are the unit vectors forming the unit cell. In the shortened form, a tube structure is fully described by the pair of integers (n,m). The absolute value of the chiral vector, the circumference, can be written as

$$|\mathbf{C}_h| = C_h = \pi \cdot d = \pi \cdot \sqrt{3}a_{C-C}\sqrt{n^2 + nm + m^2} \quad , \quad (2.1)$$

where d denotes the diameter and $a_{C-C}=0.142$ nm is the nearest-neighbour C-C distance. As an example, the chiral vector of the (4,2) tube is shown in figure 2.1. The chiral

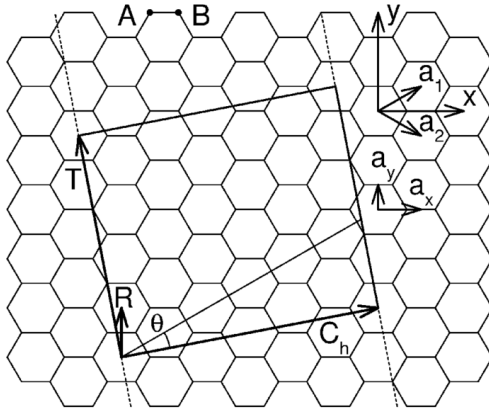


Figure 2.1: An unrolled nanotube projected on the graphene layer. The tube-structure is defined by the connection of two sites of the honeycomb lattice through the chiral vector \mathbf{C}_h [41].

angle θ ranges from 0° (zigzag) to 30° (armchair) and every value in between those two corresponds to so-called chiral tubes. The translational vector \mathbf{T} is directed along the nanotube axis and its length is defined by the shortest repeat distance (fig. 2.1). \mathbf{C}_h and \mathbf{T} bound the nanotube unit cell. With these quantities a simple expression for the number of hexagons N in the nanotube-unit cell can be obtained:

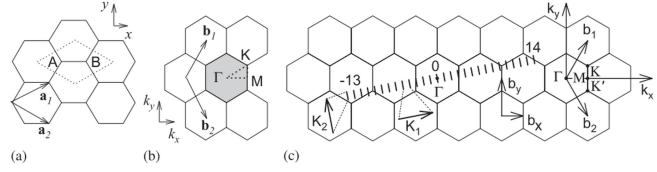
$$N = \frac{2(n^2 + nm + m^2)}{d_R} \quad , \quad (2.2)$$

2 Introduction

where d_R is the greatest common divisor between $2n+m$ and $2m+n$.

Just like in real space, the reciprocal space lattice has a (rotated) honeycomb structure. The reciprocal unit vectors \mathbf{b}_1 and \mathbf{b}_2 satisfy the condition $\mathbf{a}_i \cdot \mathbf{b}_j = 2\pi\delta_{ij}$, where δ_{ij} is the Kronecker-Delta. The collinear counterparts reciprocal space of \mathbf{C}_h and \mathbf{T} are \mathbf{K}_1 and \mathbf{K}_2 , respectively. Quantum confinement along the circumferential direction (\mathbf{K}_1) gives rise to N discrete wave vectors $\mu\mathbf{K}_1$ ($\mu = -N/2 + 1, \dots, N/2$), since $N\mathbf{K}_1$ connects two equivalent K-states as a reciprocal lattice vector of 2D graphene. These discrete values are represented by the cutting lines and are separated by $2/d$. Along the nanotube axis (\mathbf{K}_2) the k-values are continuous ($|\mathbf{K}_2|=2\pi/T$). Figure 2.2 shows the cutting lines based on the (4,2) tube. Via \mathbf{b}_1 and \mathbf{b}_2 the cutting lines can be completely transferred into the first Brillouin-zone (fully reduced representation).

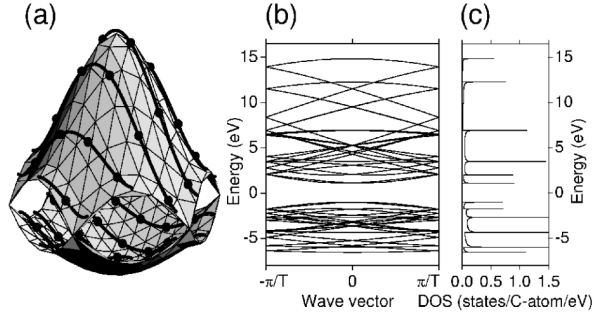
Figure 2.2: (a) Basis vectors in real space (b) reciprocal unit vectors (c) Graphene reciprocal space and cutting lines in \mathbf{K}_1 -extended representation [7].



2.1.2 Electronic structure

The zone-folding scheme now simply has to be applied to the electronic properties of 2D graphene in order to get the electronic dispersion relations $E(\mathbf{k})$ of carbon nanotubes. As the π bond between two carbon atoms features one electron, there are two energy bands that can be occupied, one valence (π) and one conduction band (π^*).

Figure 2.3: (a) The conduction and valence bands of the graphene layer in the first Brillouin zone (fully reduced representation) (b) Band diagram for the (4, 2) nanotube obtained by zone-folding (c) VHSs of the energy bands shown in (b) [41]



The left and the middle part in figure 2.3 shows the conduction and the energy-bands of the (4,2) nanotube represented by the cutting lines on the energy-surface of 2D graphene in the fully reduced representation. The energy bands and the density of states (DOS) were calculated via tight-binding calculations (ref. [41]). At the points on the cutting lines which are tangential to the equi-energy contours appear spikes in the DOS, which are called Van-Hove-Singularities (VHS). These VHSs are typical for 1D-systems. When an incoming photon matches the difference between two VHS (lower state is occupied, vertical transition), the optical absorption and emission processes show a sharp increase of intensity.

The energy values for each VHS-transition E_{ij} can be plotted against the zone-folding diameter of each individual tube chirality (Kataura plot). Figure 2.4 shows this plot¹ together with the region of laser excitation energies (green shaded area) used in this work (see chapter 6) and the tube diameters in resonance (grey shaded area).

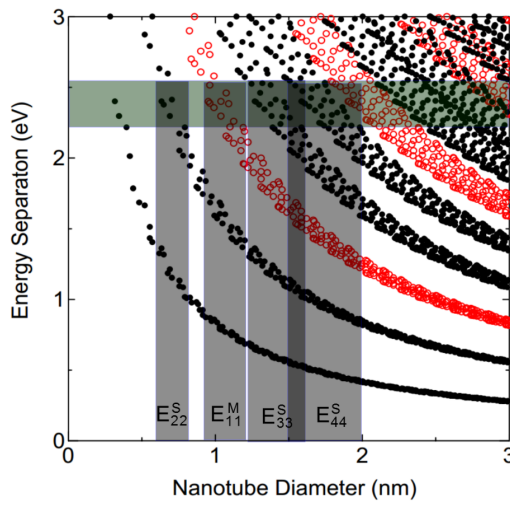


Figure 2.4: The *Kataura Plot* shows the VHS energy transitions calculated via a next neighbour tight-binding model ($\gamma_0=29.9$ eV, $a_{CC}=0.144$ nm) for each individual tube diameter. The green area represents the used laser energies and the grey area corresponds to the potential tube diameters in resonance in this work (see chapter 6 for RBM profiles). Only the energy transitions relevant for the sample analysis were highlighted by grey shading.

The Fermi level (0 eV in figure 2.3 (a)) touches the conduction band at the K-points of the graphene brilloin-zone. Subsequently, the position of the cutting lines (the nanotube structure) determines whether they cross the nearest K-point or not. If they do, the nanotube is metallic, otherwise semiconducting. This can be easily quantified by calculating the projection-length of the vector \mathbf{K} (pointing at K-point) in \mathbf{K}_1 direction: $\mathbf{K} \cdot \mathbf{K}_1 / (\mathbf{K}_1 \cdot \mathbf{K}_1) = (2n+m)/3$. Thus, if $\text{mod}(2n+m, 3)$ equals 0 the tube is metallic, if it equals 1 or 2 the tube is semiconducting. This gives rise to type I and type II semiconducting tubes.

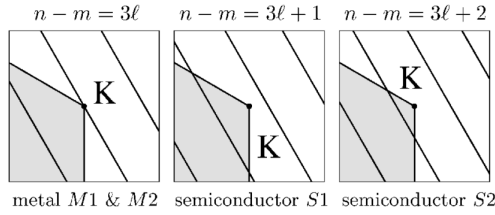


Figure 2.5: The arrangement of the cutting lines determined by (n, m) determines the metallicity of an individual nanotube. The conditions $\text{mod}(2n+m, 3)=1, 2$ or 0 (or equivalently $\text{mod}(n-m, 3)$) gives rise to two types of semiconducting and to metallic tubes, respectively [41].

In contrast to most materials where the electronic energy bands near edge-points show a quadratic dependence on k , the conduction and valence bands of the graphene layer show an approximately linear isotropic dependence near the K-points. Subsequently, the energy transitions between VHSs can also be approximated linearly by only considering

¹<http://www.photon.t.u-tokyo.ac.jp/Shoji-Maruyama/index.html>

2 Introduction

vertical transitions

$$E_{ii} = \frac{2i\sqrt{3}a\gamma_0}{d} \quad , \quad (2.3)$$

where i is a multiple of 3 for metallic tubes, and another integer for semiconducting tubes. Deviations from this linear dependence arise from the increasing anisotropy for higher energy transitions (known as trigonal warping effect) and curvature effects ($\sigma - \pi$ hybridization) for small diameter tubes. For a lot of energy transition the linear approximation already fails for the near vicinity around the K-point, especially for metallic tubes with increasing chiral angle.

2.1.3 Phonon structure

Two atoms A and B in the unit cell of the graphene layer give rise to 6 (3 acoustic and 3 optical) phonon modes, as each atom has 3 degrees of freedom. Again the zone folding scheme is applied on the phonon frequency surfaces of 2D layer graphene in order to obtain all possible phonon branches for CNTs. Figure 2.6 shows all branches and DOS of the graphene layer (a,b) and for the (10,10,) nanotube (c,d).

Not all modes are Raman active. Momentum conservation guarantees that electron scattered by phonons do not change their k-vector. Thus, only Γ -point phonons are allowed in a one-phonon scattering process (, see next section).

2.2 Raman spectroscopy

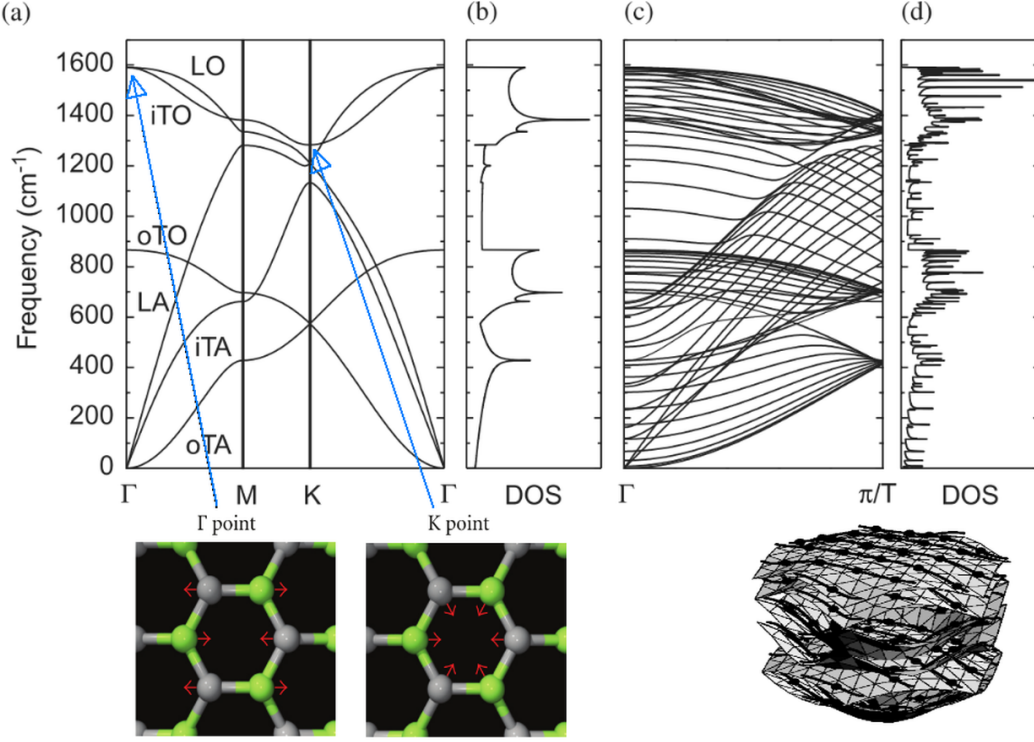
2.2.1 Raman process

Raman scattering is the inelastic scattering of light in connection with excited quasi-particle states. The difference in energy between the excitation (incident) and scattered photons corresponds to the energy required to excite a molecule to a higher vibrational mode. The Raman spectra can provide much information about the exceptional 1D properties of carbon materials, such as their phonon and electron structure, as well as information about defects of impurities.

During a scattering event (figure 2.7), (1) an electron is excited from the valence band to the conduction energy band by absorbing a photon. The excited electron is scattered (2) by emitting or absorbing phonons, and the electron relaxes (3) to the valence band by emitting a photon. Generally the energy of the scattered photon is measured, whose energy is smaller by the emitted phonon energy compared to the energy of the incident photon. The two types of emitting or absorbing a phonon are called Stokes and anti-Stokes scattering, respectively.

The number of emitted phonons before relaxation of the electron can be one, two, and so on. The order of a scattering event is defined as the number of scattering events, including the elastic scattering by an imperfection. The electron state after the scattering events is not allowed to have a different wave vector k than the initial electron state, in order to recombine with a hole (momentum conservation).

Figure 2.6: The phonon dispersion branches and the VHSs are shown for graphene (a,b) and the (10,10) SWNT (c,d). The lower insets shows the eigenvectors of the iTO Γ - and K-point phonons, respectively, and the cutting lines in the fully reduced representation [7, 13].



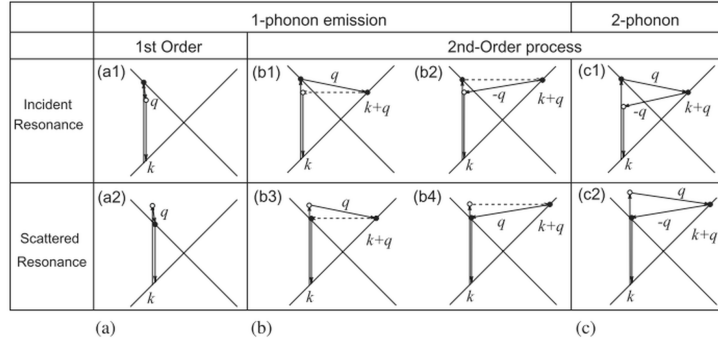
2.2.2 Stokes Raman Intensity

Within a simplified tight-binding band model, where exciton and many-body effects are ignored, the Stokes Raman intensity of a mode with energy E_{ph} varies with the laser excitation energy E_L as

$$I(E_L) \approx \frac{|J_{ii}|^2}{|(E_L - E_{ii} - i\Gamma)(E_L - E_{ph} - E_{ii} - i\Gamma)|^2} \quad , \quad (2.4)$$

where E_{ii} is the transition energy, Γ is a damping parameter and J_{ii} includes the matrix elements (optical absorption/emission and electron-phonon) and determines the maximum intensity. If it is assumed that all tubes exhibit approximately the same values for J_{ii} the (relative) intensities of the Raman peaks are given by the (n,m)-populations and the resonance conditions. The denominator of equ. 2.4 shows that either the incoming or the scattered transition is in resonance. This results in two intensity maxima for higher energy phonon modes (e.g., G-mode). The broadening factor Γ of the resonance window depends inversely on the lifetime of the excited quasiparticle state, which is influenced by environmental and temperature effects.

Figure 2.7: One and two phonon (Stokes) Raman processes are shown. If two scattering events are involved, it is called second order process.



2.3 Properties of Raman modes

The nature and the properties of the most intense Raman modes of the 2D graphene layer are shortly discussed here, as well as the rough change in their properties when the graphene is rolled up into SWNTs, and when they are exposed to pressure, tube-bundling or low doping levels.

2.3.1 Radial Breathing mode

The radial breathing mode (RBM) is the Raman signature for the presence of carbon nanotubes, related to the 'tube-breathing-like motion'. It is observed as a peak in the range of 50-760 cm^{-1} . The RBM frequency depends on the nanotube diameter d , mainly according to $\omega_{RBM} = A/d + B$. The specific values for A and B vary from report to report and are discussed in the following section. The dependence on chirality is very weak and negligible, especially for tube-diameters > 1 nm. The parameter B accounts generally for the blueshift due to environmental effects.

RBM-Intensity - probing energy transitions

As described above, the RBM frequency is very sensitive to the tube diameter d , which allows which makes it unique for each (n,m) pair. Subsequently, the energy transitions E_{ii} can be obtained by using resonance Raman spectroscopy. Temperature and pressure effects can have significant impact on E_{ii} . Increasing pressure or temperature changes E_{ii} , depending on (n,m) . For the latter, this always means a decrease, in contrast to pressure or bundling effects, which can also result in an increase of the transition energy.

2.3.2 G-line

The G-band is the main Raman signature for all sp^2 carbon materials and is related to the C-C bond stretching (Γ -Point phonon). Its generally appears around 1590 cm^{-1} .

Zone folding

Folding into a tube splits the feature into 2 components, one reflecting vibrations along (LO) and one perpendicular (TO) to the nanotube axis. Quantum confinement (cutting lines) then generates up to 6-G band peaks, luckily only two of them (referring to LO and TO, respectively) are important for Raman spectra based on unpolarized light. Decreasing diameter shifts the TO component towards lower frequencies.

Doping effects

One of the most known features of metallic SWNT is the Breit-Wigner-Fano lineshape of the lower G-band components. At certain excitation energies, the lineshape is not a simple sum of Lorentzians anymore due to phonon-plasmon interactions. Dopants now change the Fermi level can affect whether a G band spectra exhibits a BWF lineshape or not.

For this work, potential changes in Raman-shift positions are of particular interest. Indeed, low doping levels are reported to cause small blueshifts for graphene as well as for nanotubes (ref. [39, 13]).

2.3.3 D-line

The D band is the dominant Raman signature of disorder. It is observed as a peak in the range of 1250-1400 cm^{-1} and is related to the breathing of the carbon hexagons (iTO at K-point, see figure 2.6). The mode is called dispersive, as its frequency changes for varying excitation energy. It depends on the nanotube diameter as well. The excited electron state couples most probably with a phonon with wave vector $q=2k$, where k is the wave vector of the excited electron state. The intensity ratio I_D/I_G is commonly used to measure the amount of disorder, since absolute intensity measurement are generally a difficult task in Raman spectroscopy.

2.3.4 2D/G'-line

The G' or 2D mode is an overtone of the D-band, including 2 iTO K-point phonons. In contrast to the D-band, there is no elastic scattering involved in the Raman process, instead the additional K-point phonon takes care of momentum conservation. Subsequently, it is observed in the range of 2500-2800 cm^{-1} and also dispersive.

Zone folding

Folding into carbon nanotubes leads to interesting peak splitting effects. At the individual nanotube level, the specific (n,m) values get very important for the peak frequencies. The anisotropy of the graphene band structure can be directly observed for metallic tubes by quantum confinement effects in this case. $\omega_{G'}$ also depends on the tube diameter, especially for diameters below 1 nm the corresponding G' peak is significantly redshifted ([30]).

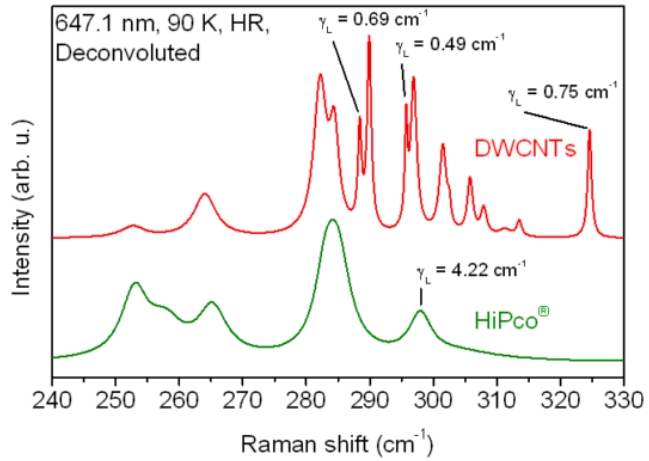
Doping effects

The G' feature can be used to assign p and n type doping in graphene and SWNTs. For substitutional n-type doping a redshift is observed because of a change in the phonon dispersion relation due to the charged dopant-defects ([21]). The relative intensity between the undoped pristine and the doped G' peaks can be used to obtain the dopant concentration. The impact on the phonon frequency is observed to be much larger for corresponding the G'-peak than for the G-band features (Γ -point phonons, ref. [39]).

2.4 Double-Wall carbon nanotubes

Double wall carbon nanotubes (DWCNTs) are another type in the family of carbon nanophases. They show a lot of very interesting properties, especially if grown by C₆₀ filled host SWCNTs (peapods). This way very clean samples can be produced and every single DWNT can be assigned to one specific inner and outer tube chirality. Selecting the host SWNTs is the most effective way to control the distribution of DWNT (or inner tube) chiralities. This is due to the fact that the inner tubes are most likely to grow at inner-outer wall distance of ~ 3.5 Å, which is caused by the Van der Waals interaction potential between the walls. However, the this optimal interwall distance is not always reached due to the chirality dependent diameter. Several outer tube diameters are possible for one specific inner tube. This holds until the outer tube diameter gets large enough for the next larger-diameter inner tube chirality. The larger the wall-to-wall gets, the less probable is the formation the corresponding inner-outer tube pair. The variation of the wall-to-wall distance leads to more narrow RBM-peaks than geometrically allowed, as the interaction change also affects the RBM-vibration energy. This is discussed in more detail later.

Figure 2.8: Raman response for the RBM of peapod-grown inner tubes (upper spectrum) compared to the response from HiPco tubes (lower spectrum). The RBM-peak linewidth γ_L of the inner tubes are about an order of magnitude narrower than their HiPco-SWNT counterparts in the lower spectrum [43].



Inner shell tubes are grown in a highly shielded environment without catalyst and are therefore highly unperturbed and defect-free. This shielding can result in a independence of the inner tubes from environmental modifications, which only the outer tube is exposed

(e.g. n/p- type doping). The unperturbed character leads to long quasiparticle-lifetimes in the inner tubes, which is reflected by the very high intensities of their RBM-modes. Additionally the temperature dependence of the intensity is a measure for the degree of lattice-defect and impurity absence ([46, 47]).

However, there are some significant differences for CVD grown inner tubes reported compared to peapod grown ones. The degree of defect-freeness (linewidths-narrowness of RBM modes) of the CVD-inner tubes is for most samples not at the level of peapod-inner tubes. Nevertheless, CVD-inner tube RBM linewidths may be at the same order of magnitude (down to $\sim 0.8 \text{ cm}^{-1}$) as their peapod equivalents ($\sim 0.4 - 0.6 \text{ cm}^{-1}$, [46, 32]). If FeCp₂ instead of C₆₀ is used as a precursor in peapods, the RBM-spectra of the samples look very similar to CVD-grown DWNTs. This gives rise to a different growth mechanism of C₆₀ based peapods compared to the other catalyst-based methods ([31]).

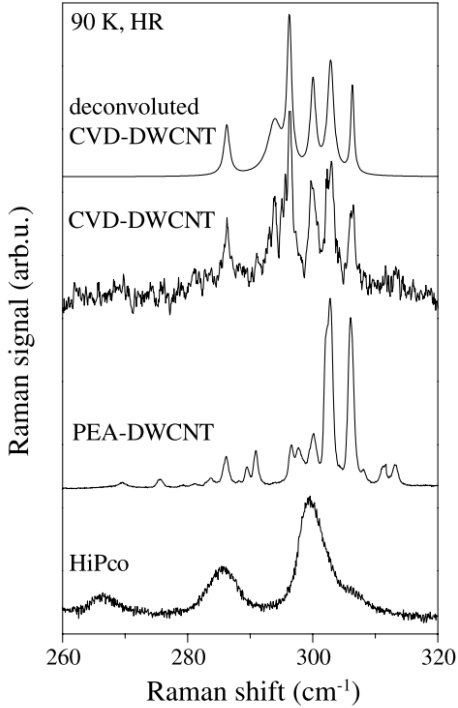


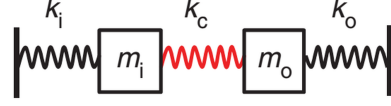
Figure 2.9: Comparison between peapod and CVD -grown inner tube RBM Raman responses. The peapod-inner tubes show a narrower linewidth and a higher intensity than CVD-inner tubes. Both quantities are measures for the absence of impurities and defects [46].

The second major difference of CVD-inner tubes is that they have a different distribution of inner-outer tube pair population. Although both growth-methods provide the same DWNT-types (reflected by the Raman peak position), the population of these types (reflected by the RBM-peak intensity) is different: CVD-grown samples tend to have more inner-outer tube combinations with larger Wall-to-Wall (WtW) -distances. This is reflected by the larger intensities of the RBM-split components at lower Raman frequency positions.

2.4.1 Collective oscillations of inner and outer tubes

Predicting RBM frequencies by computer simulations yielded better results for treating DWNT as a eigenvalue problem of two coupled harmonic oscillators rather than two individually oscillating nanotubes. As some insightful conclusions regarding RBM peak positions of DWNT can be drawn from this model, it is shortly presented here. Figure

Figure 2.10: Schematic representation of a classical coupled harmonic oscillator with 3 different force constants (k_i , k_o , k_c) and two masses (m_i , m_o).



features three different force constants. For the application of this model to DWNT, it has to be considered that all three force constants are influenced by the VdW-interaction potential Φ between inner and outer tube. The presence Φ leads to an additive modification of the force constants per unit-area k through the VdW-interaction in form of

$$k_{i/o} = k_{SWNT} + k_{VdW} = m_{i/o} \omega_{SW}^2 + \frac{\partial^2 \Phi}{\partial r_{i/o}^2} \quad (2.5)$$

$$k_c = \frac{\partial^2 \Phi}{\partial r_i \partial r_o} \quad (2.6)$$

where ω_{SW} is the natural frequency of the corresponding unperturbed SWNT and $m_{i/o}$ its mass per unit-length. The shape of Φ is discussed later. The force constants per unit length are obtained by multiplying the k 's by the circumference of the corresponding tube. For the coupling force constant per unit length, the mean diameter \bar{d} of inner and outer tube can be used:

$$K_C = k_c \cdot \pi \bar{d} \quad (2.7)$$

The normal modes ω_+ and ω_- are now the solutions of the following eigenvalue problem:

$$\begin{pmatrix} \frac{k_i}{m_i} & \frac{k_c}{m_o} \\ \frac{k_c}{m_i} & \frac{k_o}{m_o} \end{pmatrix} \cdot \begin{pmatrix} r_i \\ r_o \end{pmatrix} = -\omega^2 \begin{pmatrix} r_i \\ r_o \end{pmatrix} \quad (2.8)$$

For the sake of simplicity we now set $k_i=k_o=k$ and $m_i=m_o=m$, which gives the simplest model of two coupled harmonic oscillators possible. Although this simplification prevents useful results for the normal modes, it indicates the influence of k_c on each of them. Now the normal modes are simply

$$\omega_-^2 = \frac{k}{m} \quad \text{and} \quad (2.9)$$

$$\omega_+^2 = \frac{k + 2k_c}{m} \quad (2.10)$$

2.5 Influence of Environmental effects on the radial breathing mode (RBM)

The solutions are intuitively clear, as the in-phase oscillation of the two masses should be independent from the k_c and the counter-phase oscillation is influenced by an additional k_c for each oscillator. In principle, this also holds for the correct solutions of equation 2.8. Another very important point to note, and also featured by equ. 2.10, is that the response of each normal mode does not depend on which tube force-constant (either k_i or k_o) is changed. Each collective oscillation is influenced by the two tube force-constants equally weighted.

However, the frequencies of the two modes are not affected to the same extent by environmental influence. An environmental influence, e.g. DWNT-bundles, on these resonances depends strongly on ΔR and the absolute diameter of the two tubes. Nevertheless, the in-phase oscillation mode is influenced by a much larger extend than the higher energy counter-phase oscillation mode. Simulations of dense packed DWNT-bundles (ref. [12]) suggest a blueshift of only 1 -2 wavenumbers for outer tube diameters below 2 nm and WtW-distances ~ 0.34 nm and counter-phase oscillation. For in-phase oscillations a blueshift up to 20 wavenumbers was suggested.

Hence, for large values of ΔR (>0.35 nm) the counter-phase mode is largely independent of any environmental influences. Therefore, the higher energy mode has a very well defined vibrational frequency.

2.5 Influence of Environmental effects on the radial breathing mode (RBM)

2.5.1 Suspended SWCNTs

As described in chapter 2.3.1 the RBM vibration energy scales inversely with the nanotube diameter. This can be expressed as

$$\omega_{RBM} = A/d + B \quad (2.11)$$

where constants A and B determine the exact value of the vibration energy. Curvature effects can be neglected for tube-diameters investigated in this work, which is shown by several previous works ([16, 24]). Experiment and simulations (using various approaches) show very well agreement by assuming rolled up graphene-sheet and therefore using the ordinary elastic properties of graphene is justified.

Nevertheless, the interaction-free scaling with inverse diameter was determined experimentally by eliminating environmental effects (originating from, for instance, other tubes or the substrate). This was achieved by suspended SWCNTs grown across slits ([20]) and a scaling factor of $A=228 \text{ nm} \cdot \text{cm}^{-1}$ was derived. Of course, the additional constant B is zero, as it is the main Raman-shift correction of environmental effects. This value fits very well with first principle and continuum simulations and calculations.

Therefore $A=228$ and $B=0$ are the best values for evaluate environmental effects of a Raman RBM-feature (provided the nanotube chirality is already assigned).

2.5.2 Bundling effects

Many investigations on SWCNT-bundles provided an additional constant of $B = 10\text{-}15 \text{ cm}^{-1}$ and a scaling factor A very similar to the one given above, differing only up to 10 nm/cm^{-1} in the majority of the studies. It is very important to note that there have to be other effects taken into account that may (or may not) come along with nanotube bundling: On the one hand there is the RBM-feature blue-shift of one particular nanotube type. On the other hand there is a potential increase in the energetic distance of the Van-Hove singularities through the bundling, which means that smaller tubes are in resonance. Both effects can occur with various magnitudes, if they occur at all. There are more structural analysis methods required to distinguish between these two effects. It is suggested (e.g. [38]) that these effects depend on the degree of perfectness of register and the arrangement of the nanotube bundles.

Nevertheless, pressure experiments ([52]) and other investigations with clean nanotube bundles ([38]) propose an upshift ($=B$) up to 14 cm^{-1} for nanotube diameters above 1 nm .

2.5.3 DWNTs

DWNTs (inner and outer tube, respectively) show very interesting interaction effects. One particular inner tube type can be enclosed by various outer tube types, which implies different wall to wall distances and therefore results in different inter-wall interactions. For this reason a significant amount of RBM-resonances with a large region (up to 20 cm^{-1} or 30 cm^{-1}) can refer to one particular type of inner tube. The RBM-blueshift depends crucially on the wall-to-wall distance and therefore on each individual inner-outer tube pair ([35, 51, 17]). As described in section 2.4.1, recent works described DWNT phonon modes as a coupled (quantum mechanical) harmonic oscillator, where the coupling constant k_c contributes (in addition to the spring constants of the individual inner and outer tubes k_i , k_o) to the vibrational energy ([19, 12, 54]). This quantized model also shows that quantum interference can play an important role in order to understand the observed resonances. This approach achieves good results for a simple continuum model ([24, 28, 12]), which ignores the atomistic nature of the tubes. In general, the model of a coupled oscillator provides a better prediction of RBM frequencies than individually oscillating inner/outer tubes. Therefore, intense and narrow RBM peaks designated as 'inner tube resonances' should be renamed collective inner-outer counter-phase resonances. Analogous, 'outer tube resonances' should be renamed to inner-outer in-phase resonances.

The range of the splitting depends strongly on the production process. Peapod-grown inner tubes show a much wider splitting range and much smaller mean diameter than (less defect-free) CVD-grown inner tubes. Therefore chemical vapour deposition is the more selective method for large-diameter DWNTs, which is an advantage for the investigation of individual inner-outer tube pairs.

Van der Waals interaction potential in DWNTs

The modification of the nanotube RBM-vibration energy through the presence of an outer (or inner, respectively) has been tried to be calculated by various (more or less) different approaches (e.g. [28, 24, 51]), including ab-initio calculations ([23]). However, DFT ab-initio calculations could not yet provide the needed accuracy of reproduce the attractive Van-der-Waals interaction and subsequently the modification of Raman feature vibration energies.

Ignoring the ab-initio calculations, the interaction potential between two points at a distance r on different shells has always the form

$$V(r) = 4\epsilon \left[\left(\frac{\sigma}{r} \right)^{12} - \left(\frac{\sigma}{r} \right)^6 \right] \quad (2.12)$$

where $\epsilon=2.964$ meV (energy-pot minimum) and $\sigma=0.3407$ meV (zero-point) are taken from literature. This potential has to be integrated in a proper way in order to obtain the full interaction potential Φ . There are several approaches to accomplish this task, each one has its specific advantages. The simplest approach is a continuum model, which ignores the atomistic nature of nanotubes (chirality). The detailed shape of the interaction potential of concentric nanotubes is still a topic of current research.

The main factor determining the curvature of the interaction potential Φ , ignoring potential impact of absolute diameter, is the wall-to-wall distance ΔR . The region around the minimum of $\Phi(\Delta R)$ (maximum curvature) is reflecting the most probable interwall distances. However, the growth of DWNTs with large ΔR (>0.4 nm) is still possible according to ab-initio calculations ([23]) and direct observation via HR-TEM measurements ([18]). The quantities Φ and $\partial^2\Phi/\partial d$ can be calculated and measured. For instance, Φ

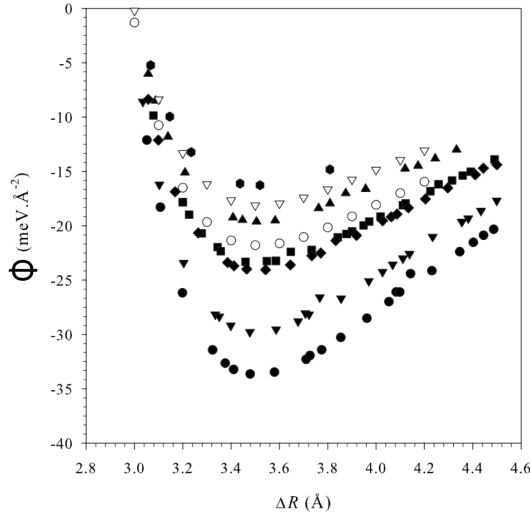


Figure 2.11: Dependence of interaction energy Φ on the wall-to-wall distance ΔR plotted for various inner-outer tube combinations. The different black symbols refer to one specific inner tube chirality. The white symbols refer to continuum model calculations with different inner tube diameters. It can be seen that for ΔR beyond 3.8 Å $\Phi(\Delta R)$ gets more and more linear [51].

has been calculated for a large sample of DWNT chiralities in ref. [51] by summation of the Lennard-Jones interaction (equ. 2.12) over atomic pairs. Also an analytical expression of the interaction potential has been derived, similar to previous studies ([34, 12]).

2 Introduction

The results of ref. [51] are shown in figure 2.11. These plots of the interaction potential are suggesting a minimum with maximum curvature at ~ 0.34 nm and a vanishing curvature $\Delta R > 0.38$ nm.

The second derivative of $\Phi(\Delta R)$ can be measured by pressure experiments on graphene layers (and extrapolations to negative pressure regions ([19])). It can be seen here that this quantity (and therefore the coupling constant K_{VDW}) is getting rapidly closer to zero for increasing wall-to-wall distance. Further extrapolation to ΔR around 4 Å suggest a negligible influence of k_{VDW} on $k_{i/o}$ (equ 2.6).

3 Experimental setup

3.1 General Raman spectrometer

The schematic structure of a general Raman spectrometer is very simple. A tuneable laser (e.g. Gas-laser) with a small band-width is focused on a specimen. The scattered light is collected with a lense and guided through a monochromator to select a specific energy area. The most popular experimental configuration is the so-called backscattering geometry, where propagation of the scattered light differs $\sim 180^\circ$ from the incident light.

The energy dispersion of the scattered photons is realised through gratings. The density of nodes and the size of the illuminated area of the gratings determine the resolution power of the spectrometer (in addition to the number of gratings, of course). As the energy shift is measured in wavenumbers, the resolution power determines the minimal detectable wavenumber shift between two pixels of the detector.

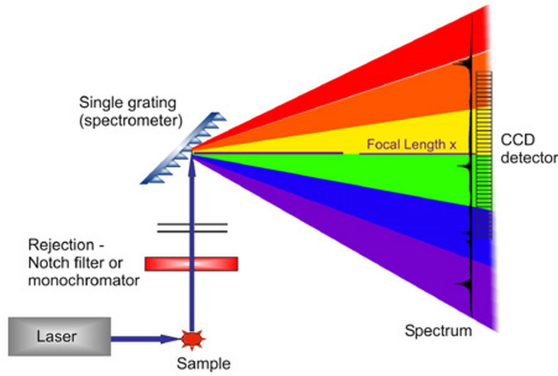


Figure 3.1: Simplified picture of an general Raman Spectrometer with one diffraction grating

3.2 Dilor XY 800 - Raman Spectrometer

The *Dilor XY 800* Raman Spectrometer was used for the measurements here and has in principle the same operation structure as described above. However, as figure 3.2 shows, the exact structure is a bit more complicated. The spectrometer can be operated in normal or in high resolution mode.

Different laser sources (in our case Argon-Krypton gas or a dye-laser) with a narrow band width can be used for dispersive Raman measurements. The laser light is focused via an regular objective (focal length ~ 4 cm, NA=0.5) onto the surface of the sample. The backscattered light is collected through a system of lenses and focused on the position of the first slit (opened $100\ \mu\text{m}$). This slit reduces the intensity of the scattered light

3 Experimental setup

and the illuminated sample area. The first concave mirror (M1) parallelizes the light and illuminates the first grating (G1). The position of the focus of the second mirror (M2) determines whether the spectrometer operates in normal or in high resolution mode. The focus is not changed by the mirror M2, but an additional moveable mirror can guide the light through an additional path.

Normal resolution

In normal resolution mode this mirror does not influence the path of the light and the focus of the second mirror is positioned in front of the third mirror (M5). At a position near the focus the beam passes the second (opened) slit in order to select a passband. The third mirror refocuses the beam on a second grating (G2) and a subsequent mirror (M6) parallelizes the light again, which then passes through the third slit (S3). Like the first slit, this slit is closed and improves the resolution of the observed peaks. Then the light passes through the last mirror-grating-mirror system (M9, G3, M10), which is called *Spectrograph*. So this last (third) grating is the actual place where the dispersion of the scattered light happens in normal resolution mode. The first mirror-grating-mirror system is called *Foremonochromator*. The distance between the last grating and the last mirror represents the focal length of the spectrograph in normal resolution mode. The last mirror parallelizes the light again and a corresponding lens focuses the dispersed light to the liquid N₂-cooled silicon stripe-detector.

High resolution

In high resolution two important things are different. First, as mentioned above, a moveable mirror guides the light through an additional path. That changes the position of the focus of the second convex mirror. Second, the third slit is opened. Due to the changed focus, the third concave mirror (M5) now parallelizes the light and it is dispersed through the second grating. With the third slit opened, all gratings now contribute to the dispersion of the light. So there are now three focal lengths determining the dispersion.

3.3 Issues spectrometer position control

The software *LacSpec* communicates with the detector and with the position of the spectrometer in order to provide a correct Raman-spectrum. As this communication lacks reliability, the spectrometer and the input position have to be readjusted by known gas lines. There can be various reasons for the discrepancy, mostly the finite accuracy of the spectrometer position control adds up to a significant error when the spectrometer is moved multiple times.

If this has to be done precisely for the whole spectrometer range, the spectrometer has to be moved from zero-position to the maximum central wavelength position. This requires a non-negligible amount of time and is therefore not performed before every measurement.

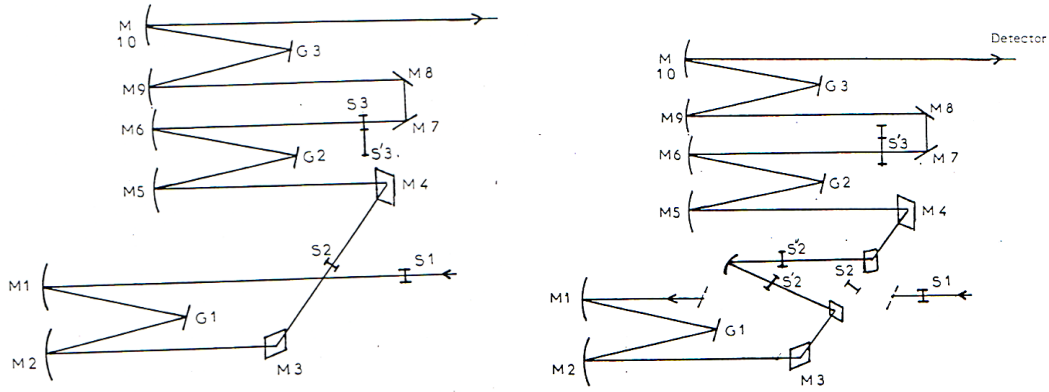


Figure 3.2: The light path of the Dilor XY Raman-Spectrometer in normal (left) and high resolution mode (right)

For this reason, the spectrometer often is only adjusted near the zero position, as it takes a lot of time to do this for the whole spectrometer range. As a result, the miscommunication often enhances with larger spectrometer-position (= larger reflection angle). In this case a recalculation of the Raman-shift values after the measurement is even more advantageous for high Raman-shift features. In the next chapter the detailed post-measurement calibration process is described.

3.4 Calibration lamps

The calibration lamps by LOT-Oriel (*Pen Ray*) provide a wide range of narrow well-defined gas lines of various noble gases. Four different lamps were available, containing Neon, Argon, Krypton and Xenon, respectively. Of course, the lamp-lines are only useful if they are correctly assigned to a wavelength in a database. The figure 3.3 shows the positions of the correctly identified strong lamp lines over a large Raman-shift range for 400 nm laser excitation wavelength.

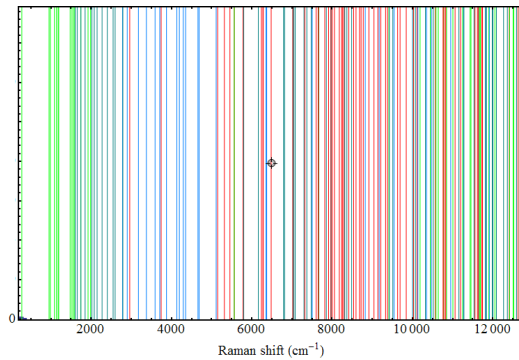


Figure 3.3: Spectral Position of identified noble gas lamp lines for $\lambda_l = 400$ nm. Neon is red, Argon is green, Krypton is turquoise, Xenon is blue and Mercury is ochre.

3.5 Lasers

3.5.1 Argon-Krypton gas laser

The gas laser model *Coherent Innova 70C Spectrum* was used for the sample analysis. A mix of Argon and Krypton provided a big range of gas lines for different laser excitation energies.

Table 3.1: Argon-Krypton lines available for laser excitation energy (wavelength) E_l (λ_l)

Available gas lines for Ar-Kr laser			
Argon		Krypton	
λ_l (nm)	E_l (eV)	λ_l (nm)	E_l (eV)
465.790	2.66	468.041	2.65
487.986	2.56	520.832	2.38
501.716	2.47	530.866	2.33
514.530	2.41	568.188	2.18

3.5.2 Dye-laser

A dye laser uses the advantages of a nearly continuous spectrum of its dye. The advantage is the possibility of tuning the laser excitation energy accurately in little steps. Therefore the noble gas energy transitions are not required, in contrast to the mixed gas laser). For a dye laser the laser energy is selected by a birefringent tuner. Two different dyes (*Rhodamine 6G* and *DCM special*) provide a large spectral range around the yellow (~ 560 nm) and red (~ 650 nm) spectrum region. For calibration studies in this work the *model 599* by *Coherent* was used. For good emission rates the dye had to be illuminated by an intense pump-laser (1 Watt maximum beam power).

Due to the continuous spectra of the dyes the laser excitation wavelengths are not known with the same accuracy compared to a mixed noble gas laser. This could be a problem for high resolution Raman shift features and requires accurate pre and post measurement calibration of the Raman shift scale. This issue for Dye lasers is discussed in the section 4.4.

3.6 Set of studied samples produced by no-flow CVD

The grown nanotube arrays on quartz-plates were produced with a no-flow CVD process, as described in ref. [56, 50]. A binary Co/Mo catalyst was loaded onto the substrate (dip-coating). During the heating of the CVD-system Argon gas containing 3% H_2 was introduced at a flow rate of 300 sccm and a pressure of 40 kPa in order to reduce the metallic catalyst particles. After the growth temperature of 800 °C was reached, the system was evacuated and the feedstock (40 μ L) was introduced all at once. The feedstock was a mixture of ethanol and acetonitrile (CH_3CN). As presented in table 3.2, the CVD reaction time and the acetonitrile concentration in the feedstock varied among

the studied set of samples. After synthesis, the reaction chamber was evacuated and cooled while flowing 300 sccm Argon.

Table of studied CVD-grown samples deposited on a quartz substrate		
Acetonitrile share in feedstock	Deposition/Reaction Time	Estimated sample thickness
0%	65 s	8-10 μm (semi-thick/still transparent)
	75 s	8-10 μm (thin/very transparent)
	7 min	> 50-70 μm (thick/not transparent; black carbon material)
3%	3 min	20-30 μm (thick/almost not transparent)
5%	7 min	> 50-70 μm (thick/not transparent)

Table 3.2: All samples were produced, as described precisely in [50], by the CVD-method with a Co/Mo Catalyst deposited on a quartz substrate. The thickness of the sample depends on the Reaction/Deposition time and on the amount of the added feedstock (pressure in vacuum chamber). In [50], all investigated samples were produced with a Reaction time of 3 minutes and adding feedstock of 40 μm (constant pressure in vacuum chamber). The sample thickness was estimated by the transparency and comparison of nanotube films on quartz substrates in ref. [56].

3.7 Experimental details

The power of the laser beam onto the sample was kept constant at ~ 0.9 mW in order to avoid temperature effects and to keep the intensities as consistent as possible.

In NR mode, one measurement-cycle collected the intensity (number of counts per pixel) over 30 seconds. The final spectra was an average over 20 measurement cycles, which were (most times) sufficient to reduce the signal noise to a negligible level. In HR mode, 120 measurement cycles were necessary to accomplish this (also with 30 seconds accumulation-time).

4 Calibration

4.1 The calibration problem

The position of a Raman-Spectrometer is a very sensible quantity, as it depends of the position of various (in case of the *DilorXY* 800 Spectrometer three) gratings. Therefore the real position is never exactly the same every time it is moved, although the input position is the same. The spectrum has to be rescaled through calibration lamps, such as Neon, Krypton, Xenon and others. The positions of the emitted lines of these Lamps are well known and saved in the NIST Internet-database ¹. For every observed spectral window one has to find a lamp among these, which has at least one spectral line in it. The presented method below makes a reasonable calibration with only one spectral line possible, as the dispersion and the spectral range at the corresponding energy region is calculated by it. Of course, a correct identification of the observed spectral lines is the requirement to do this.

As this takes much effort to do for every measurement, a method is presented here to calibrate a measured spectrum after the measurement. To do this the spectral window and the wavenumber shift per pixel of the detector, which operates in our case with 2048 pixels, has to be calculated. The wavenumber value for every pixel has to be rescaled by comparing the calculated position of the measured spectral peaks of the lamps with the position of them from the database. By changing geometrical values move the calculated peak-position in such a way that calculated and database position finally overlap. The method to calculate wavenumber shift values is presented and discussed below.

4.2 Calculation of Raman shifts and spectral range

4.2.1 The grating equation

Our aim is to calculate the wavenumber-shift values for every pixel of the detector, when some values of the spectrometer geometry are given. These values are the initial focal length F , the groove density of the grating n , the Number of pixels N and the initial diffraction angle for the central position β .

The grating equation determines the dispersion between the diffraction-angle β and the wavelength λ (nm).

$$\sin \alpha + \sin \beta = 10^{-6}kn\lambda$$

Here k denotes the diffraction order and n (1/mm) the node density on the grating. The difference between the incident-angle α and the diffraction-angle β is independent from

¹<http://www.nist.gov/pml/data/index.cfm>

the position of the grating and remains always the same. Therefore the grating equation can be rewritten with the constant (see figure 4.1) $D_V = \beta - \alpha$:

$$10^{-6}kn\lambda = 2 \sin \frac{\beta + \alpha}{2} \cos \frac{D_V}{2} \quad (4.1)$$

We only consider the first diffraction order in our calculations. Therefore we can rear-

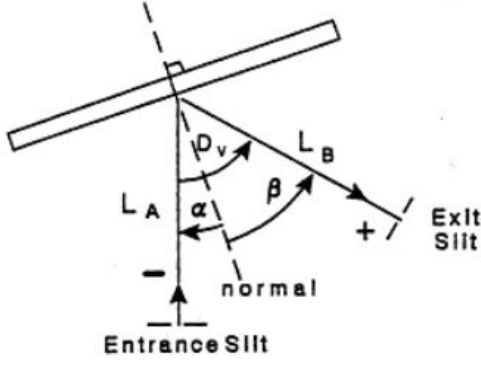


Figure 4.1: Geometry used for the presented recalculation of the Rama-shift values for every pixel

range equation 4.1 to get β :

$$\beta = \arcsin \left(\frac{10^{-6}n\lambda}{2 \cos (D_V/2)} \right) + \frac{D_V}{2} \quad (4.2)$$

4.2.2 Rescaling of the wavenumber-axis

For our spectrometer the groove density n equals 1800/mm. So we need for the calculation of β the deviation-angle D_V (deviation through grating) and the wavelength of the central position of the spectrometer λ .

In order to calculate the wavenumber-shift for every pixel we also need the deviation angle δ from the central position (diffraction) angle β . δ_p is calculated from the triangle formed by the focal-length F and the distance from the target pixel to the central pixel. One pixel has a length of 13 μm .

$$\delta_p = \arctan \frac{p \cdot 13 \mu\text{m}}{F} \quad (4.3)$$

p denotes the pixelnumber and has a range of -1023 to 1024. With equation 4.1 we can now calculate the wavelengths or wavenumbers for every pixel by adding δ_p (corresponding to pixel p) to the diffraction-angle β .

4.2.3 Linear dispersion or resolving power

Linear dispersion $dx/d\lambda$ ($x = p \cdot 13 \mu\text{m}$ for the stripe detector in use for this work, see equ. 4.3) is the distance parallel to the detector plane, is associated with an instruments

4 Calibration

ability to resolve fine spectral detail. The inverse angular dispersion is simply obtained by the first derivative of the grating equation with respect to β :

$$\frac{d\lambda}{d\beta} = \frac{10^6}{kn} \cos \beta$$

The inverse of this quantity (=the actual angular dispersion) is a good measure of how well the light can be dispersed by the experimental configuration independent of the focal length F . With $dx = d\beta \cdot F$ the linear dispersion defined above takes the form

$$\frac{dx}{d\lambda} = \frac{kn \cdot F}{10^6 \cdot \cos \beta} \quad (4.4)$$

where $d\lambda$ denotes the resolvable wavelength-difference determined by the Rayleigh-criteria.

4.2.4 Application and Implementation

Directly after every measurement of a Raman-spectrum it is necessary to measure the lines of an appropriate lamps (depending on the wavelength of the observed modes) without moving the spectrometer. Then this spectrum of the lines is plotted by a program (e.g. Mathematica) together with the well known position of the lines of various lamps from a calibration file, which assigns a line position to the corresponding lamp. The content of the calibration file is plotted in figure 3.3.

As described above, the program now calculates the new wavenumber shift values for every pixel with a given initial set of geometrical values (D_V , F and β) and plots it in the same diagram. Rough values for D_V and F have to be known (e.g. from manual, measurements). The initial value for the diffraction angle β is calculated through equation 4.2. The central wavelength λ in this equation corresponds to the given wavenumber shift of the central pixel (i.e. the 1024th pixel of the detector) at a certain laser-wavelength. The wavenumber value of the central pixel does not depend on the dispersion and is therefore also independent from the focal length F . If the values for D_V and F are approximately correct, the calculated spectrum should therefore roughly match the initial plot of the spectrum. If this is not the case despite correct geometrical values, the reason is probably an unequal central pixel assigned to the calculated and the original spectrum. This is due to not used pixels of the detector during a measurement. Not every RBM measurement uses the full range of available pixels, depending on the alignment of the spectrometer software. Therefore also the correct central pixel has to be found for the calculated spectrum.

A program which executes the operations above now has to allow a manipulation of the diffraction angle β , the focal length F and the central (or first used) pixel number. The initial, the calculated spectra as well as the lamp lines have to be plotted in one diagram. Then adjusting the focal length F for an almost equal dispersion should make it easy to find the correct central pixel by overlapping the calculated and the original spectrum (providing the initial parameters D_V , λ_L , n are correct). The original spectrum should be easily reproduced this way.

4.3 Application on the Dilor XY Raman spectrometer (noble gas laser)

By varying the diffraction angle β the position of the lamp spectrum can now be adjusted to match the lines of the corresponding lamp from the lamp-line datafile. The deviation of the reflection angle β between the two spectra reflects the error of the detected spectrometer position. Eventually the dispersion can now be readjusted if necessary (providing there are more than 2 strong lamp lines visible in the observed spectral window). This is especially useful for HR-measurements.

Now the actual Raman-spectrum intensity values can be loaded into the just derived Raman-shift axis values. Of course, the reflection angle β should not be recalculated by this process. The Raman spectrum can now be exported as a proper datafile format (to avoid confusion with the original datafile, e. g. *.cal*, *.dat*, ...).

This features were realised with the *Manipulate* command of the computer-algebra program *Mathematica*. Of course, the description above can be applied to a lower level programming language to provide a greater compatibility with other platforms (e.g. Java for independence of operating system). However, in this work all calibrations were performed with a Mathematica-script.

4.3 Application on the Dilor XY Raman spectrometer (noble gas laser)

4.3.1 Problem of simplification in HR-mode

The equations used for the calibration methods assume a very simple geometry with only one diffraction grating (figure 4.1). As described above, the Raman-Spectrometer DilorXY however uses several additional gratings and mirrors to guide the scattered light to the detector. The question arises, whether the use of the simple calibration method is justified.

We have to distinguish between normal and high resolution mode. In normal resolution mode the dispersed light is focused on the last mirror, whereby the focal length can be considered as the distance between the mirror and the detector. So the structure is the same as in our simplified picture and the value of the focal length F directly corresponds to a real counterpart.

In the high resolution mode the situation is slightly different. Except for one additional mirror, the light passes the same gratings and mirrors as it does in normal resolution mode. The important difference is that the scattered light is not focused the same way on the mirrors as it was before and the third slit is now open. Now each of the three consecutive gratings contribute to the dispersion of the scattered light. Therefore we would have to evaluate the grating equation 4.2 three times in a row with three different focal lengths to calculate the new wavenumber axis. If we use only one grating equation though we now use an effective focal length, which does not correspond to real one. The theoretical possibility of an effective grating-node density is ignored here. The comparison of calibrated high and normal resolution mode spectra should show if the calibration method is accurate enough for high resolution calibration.

It should be mentioned that although the dispersion and resolution power is increased

in high resolution mode, the wavenumber-shift value of the central pixel ($p=0$) should remain the same, as it is independent of any increase of dispersion.

4.3.2 Difference in calibration accuracy between NR- and HR-mode

Of course, the Raman Shift error with respect to the spectral range becomes bigger in HR mode. Although the absolute error in wavenumbers does virtually not change in comparison to NR mode, this is a 'problem': The position of the Raman features gain relevance in HR-mode, as broadening effects are significantly reduced and distinct Raman features are dispersed better. This means that high resolution spectra require a more accurate calibration in absolute wavenumbers. In contrast, for NR-measurements such an accuracy in calibration makes no sense/is not possible, as the error through limited resolution power would be much higher than the error through calibration/geometrical parameters. Therefore a Raman-shift error *with respect to the spectral range* is a quantity that reflects an adequate measure for pre-measurement calibration accuracy for NR and HR mode, respectively. The extent of the correction of this relative Raman shift error now characterizes impact on the adequate accuracy of the post-measurement calibration in relation to the pre-measurement calibration. Thus, a correction through the post-measurement calibration method is even more valuable in HR- than in NR-mode.

4.3.3 Consistency tests

In order to test consistency between high and normal resolution mode calibration and prove accuracy of the method, Raman-spectra at different laser excitation energies are plotted (fig. 4.2). To demonstrate the differences between calibrated and uncalibrated spectra shifts of spectral lines of calibration lamps are plotted in the RBM region as well (fig. 4.3). Of course, the accuracy of the uncalibrated spectra depends on the pre-measurement calibration of the spectra calculated by the measurement-managing software. In our case the spectrometer-software was calibrated in low shift (RBM) region ($\lambda_l=568.188$ nm). Therefore, post-measurement calibrated RBM spectra should show only very little deviations from original spectra if any deviations exist at all. After all a usual pre-measurement calibration should also provide a reliable and accurate Raman-shift scaling. However, with the presented post calibration method we can improve accuracy and reliability, which is a central aspect of slight Raman-shift sensible physical features.

In high resolution mode an effective focal length has to be found in order to reproduce a high resolution Raman-shift scaling. Of course, RBM features should hold the exact the same position, when a high and normal resolution spectrum of the same sample is compared. At least in the RBM region an effective focal length should be found where no difference in dispersion in relation to the lamp line positions from the datafile is observed. For this reason two different laser excitation wavelengths (487.986 and 568.188 nm) have been used to test the reliability of an effective focal length for RBM spectra. This region provides the most interesting applications for high resolution mode measurements.

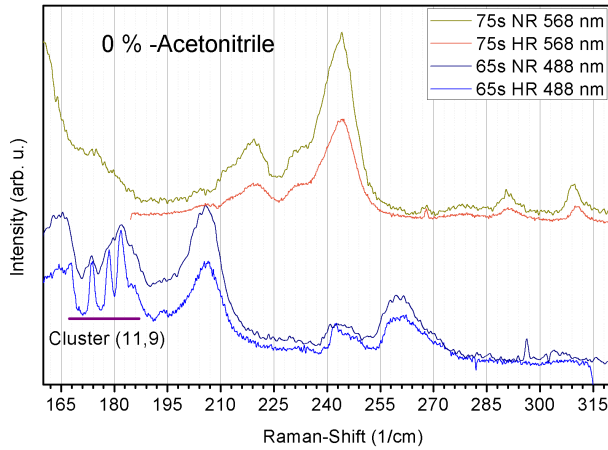


Figure 4.2: RBM modes of two thin 0% samples (65s and 75s deposition time) measured in normal and high resolution mode. The reduced noise and better resolving power makes quantifying Raman-shifts more reliable in HR-mode than in NR mode. On the bottom left an early growth stage of DWNT (11,9)-cluster (studied in detail in chapter 6) can be resolved in HR-mode.

In figure 4.2 we can see the RBM spectra of thin CVD-grown samples (0 % acetonitrile) at 568 and 488 nm laser wavelength each in normal and high resolution mode. Calibration lamps were used after every completed measurement, as the spectrometer was always moved. The spectra show that high and normal resolution measurements are very consistent in Raman feature position. As expected, no inconsistencies could be discovered in the RBM-region due to the existence of an effective focal length. Although this is just an example for the calibration of post-measurement high resolution spectrum, there should not appear any problems of using this one-grating recalibration, assuming the equivalence of increasing resolution power by increasing the focal lengths and adding diffraction gratings.

Although the focal length should not change once a proper one has been found, it may be that the effective focal length has to be adjusted for different spectrometer positions for high resolution measurements. It is assumed here that the wavelength of the monochromatic laser is known here with sufficient accuracy (e.g. gas laser $\Delta\lambda_l = \pm 5 \cdot 10^{-4}$ nm).

The impact of the errors in pre-measurement spectrometer-calibration strongly depend on the resolution power of the experimental setup and therefore the correction through the post measurement calibration method is even more valuable in HR mode, as explained above. This is shown in figure 4.3, where the increase of the *relative* Raman-shift error is directly observable. Another aspect of this figure is the readjustment of the effective focal length after correction of the reflection angle β for the HR-measurement. While the original spectrum could be exactly reproduced by using a focal length of $F=1560$ mm, the dispersion was not displayed correctly considering two lamp line positions from the lamp-datafile. It had to be readjusted to 1544 mm. This reflects the need of two visible calibration lamp lines in the spectral window of one spectrometer position in HR-mode. In contrast, for the NR measurement there was no readjustment necessary.

The error increase for increasing Raman shift (=distance between two spectrometer positions) is demonstrated in figure 4.4 below. As mentioned above, the spectrometer-software was calibrated with the help of the laser line and a calibration lamp line in the

4 Calibration

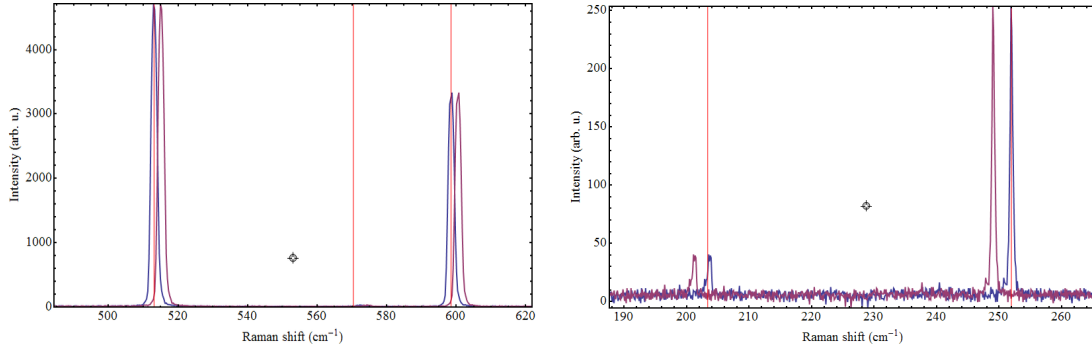


Figure 4.3: The deviations in absolute wavenumbers are only a little larger in the high resolution measurement (right) due to a different calculation of the Ramanshift-scale of the spectrometer software. In relation to the spectral range this error gets much more significant, however. In normal resolution the dispersion was calculated correctly (in contrast to reflection angle), whereas in high resolution it had to be slightly corrected by adjusting the (effective) focal length with help of two neon lamp lines.

RBM region only before the measurement.

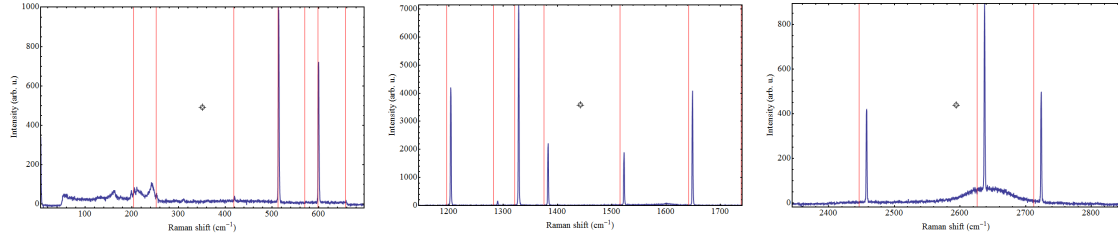


Figure 4.4: The 3 shown lamp spectra at different Ramanshift regions recorded with the pre measurement calibrated spectrometer software demonstrate the increase of the error of the reflection angle of the Raman shift scale. The dispersion of all 3 spectra could be reproduced correctly for a focal length F found at 578.04 mm. Therefore only the reflection angle had to be corrected

4.3.4 Estimation of resolution power/accuracy of calibration in HR mode

The resolution power mainly depends on the accuracy of the lamp line positions and their FWHM. Naturally, this improves the accuracy of the adjusted Raman scales, if their corresponding lamp lines are measured in HR-mode. This is a consequence from the fact that the resolution power or the linear dispersion is linearly proportional to the focal length F for constant wavelength (see equ. 4.4). For the Dilor XY spectrometer used for the analysis in this work, this means an improvement of resolution power in HR-mode by a approximate factor of 3 compared to NR mode. What means this improvement of resolution power for the magnitude of a practical modification in wavenumbers of a post-measurement calibrated Raman-shift scale? This is demonstrated by two RBM-spectra, one in normal, one in high resolution mode. The lamp -lines of these two spectra are shown in figure 4.3. Figure 4.5 shows the corresponding inner tube cluster RBM-spectra (cluster (10,7), detailed analysis later), which are very suitable to demonstrate a difference

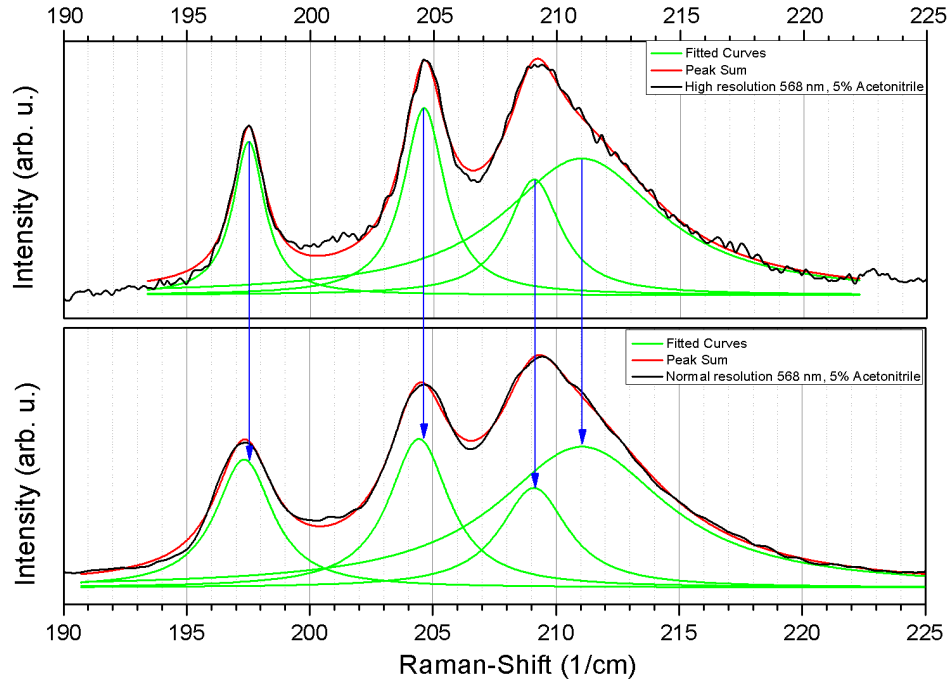


Figure 4.5: RBM lineshape in HR (upper panel) and NR (lower panel) for the same RBM feature (DWNT-inner tube cluster). The blue vertical arrows indicate the position of the Lorentzian-fitted split components in the HR-spectrum. In the larger spectral window in NR mode two additional gas lines compared to the HR mode-window were observed. The accuracy limit in NR mode explains the observed slight deviations in positions of the observed RBM spectra.

4 Calibration

in RBM-shift positions of the peaks, as they (the split components) have a very narrow linewidth. This difference turns out to be 0.2 cm^{-1} maximum, and is not constant for the individual split components in particular. Despite the fact that there were more gas lines available for calibration in NR mode, the resolution limit of the latter is the reason for the deviations.

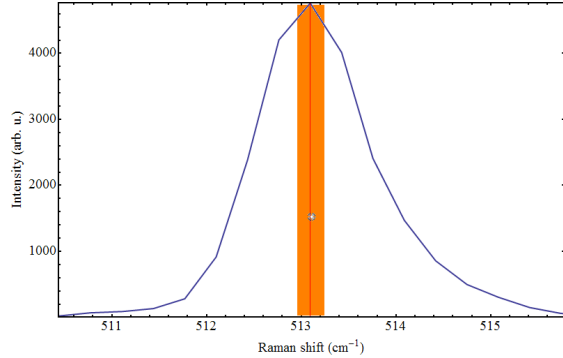
Table 4.1 shows the obtained focal lengths for the Dilor XY Raman spectrometer, as well as the average change in Raman shift $d\omega$ per pixel (for NR and HR mode, respectively). Of course, this change is determined by the dispersion and therefore by the spectral position of the two corresponding pixels and the given values are just rough averages. Nevertheless, values allow to create an arbitrary confidence interval for the absolute accuracy of the calibrated Raman scale for NR or HR mode. Together with a symmetric lamp line, the Raman-shift position can be determined accurately by an arbitrary interval. In fact, the symmetry of a calibration lamp line can help to improve the Raman-scale accuracy slightly beyond $d\omega/dx$, as shown in figure 4.6. The interval defines a Raman scale accuracy of $\sim 0.3 \text{ cm}^{-1}$ at $\lambda_l=568.188 \text{ nm}$ for the DilorXY spectrometer in NR-mode.

The corresponding interval in HR-mode can be set at $\sim 0.1 \text{ cm}^{-1}$.

Table 4.1: The focal lengths to reproduce the pre-measurement calibrated spectra (F_{pre}) and to the overlap lamp lines with the datafile values (F_{post}) do not differ in NR mode. They work for the Dilor XY spectrometer at all laser wavelengths. $d\omega/dx$ denotes the average wavenumber change per pixel. Of course, this quantity depends on the spectrometer position.

Dilor XY Raman Spectrometer @ 568.188 nm		
	NR	HR
$F_{pre} \text{ (mm)}$	578.04	1560
$F_{post} \text{ (mm)}$	578.04	1544
$d\omega/dx \text{ (cm}^{-1}/\text{px)}$	0.35	0.13

Figure 4.6: The arbitrary confidence interval (orange area) determines the Raman scale accuracy. The width can be set as $\sim 0.3 \text{ cm}^{-1}$ (NR, 568.188 nm, Dilor XY), which is below the Raman shift step per pixel $d\omega \sim 0.355 \text{ cm}^{-1}$. Providing a correct focal length (can be checked by other lamp lines), any change in Raman shift above $\sim 0.3 \text{ cm}^{-1}$ now can be confidently quantified.



4.4 Dye-Laser measurement calibration

The calibration of a spectrum derived using a dye laser is a bit more delicate, as the zero-shift position (laser wavelength) is often not known with the necessary accuracy

for a precise Raman spectrum. In our case the birefringent tuner by micrometer screw only allowed a tuning of the wavelength with the bad accuracy of about ± 1 nm. Of course, one has to improve the accuracy by aligning precisely the zero-shift position with the center of the laser beam Lorentzian (after putting some attenuators into the laser). In theory the laser wavelength can be determined very accurately ($\sim \pm 0.001$ nm), but the detected spectrometer position is many times (as for the *DilorXY*-spectrometer used here) not a reliable quantity. As mentioned in the previous chapter, small errors in the detected position every time the spectrometer is moved are adding up to a significant error. Therefore a known spectral line of a calibration lamp within the spectral window of the zero-position is necessary to tell the spectrometer its positioning. However, if there is no noble gas line within the spectral window of the laser position (or somebody forgot to measure it), there is still a accurate calibration possible by moving the spectrometer to a low Raman shift region (e.g. RBM) and measuring the gas lines here. Then, only the error of the difference of the two spectral positions of the central pixel has to be ignored, not the absolute error of the laser line position.

So the spectral distance between the zero shift position and a low Raman shift position ($100\text{-}300\text{ cm}^{-1}$, RBM-region) is the quantity which is much more reliable and stable in time than the absolute spectrometer position. A prerequisite for finding the wavelength this way is a accurate pre-measurement calibration of the spectrometer software in order to make errors of individual spectrometer movements to low shift-regions negligible. Therefore a Raman shift error of the central pixel in the RBM-region (determined by the reflection angle β) cannot be considered then, as the correct wavelength has got to be found first. Of course, finding the correct wavelength is important, especially considering this results in a corrected dispersion of the Raman scale.

4.4.1 Application

The first step of a reasonable calibration is reproducing the measured the spectrum, which shall be calibrated. The assumed wavelength has to be listed (e.g. in the name of the created ASCII-file), as this is the wavelength we first have to work with.

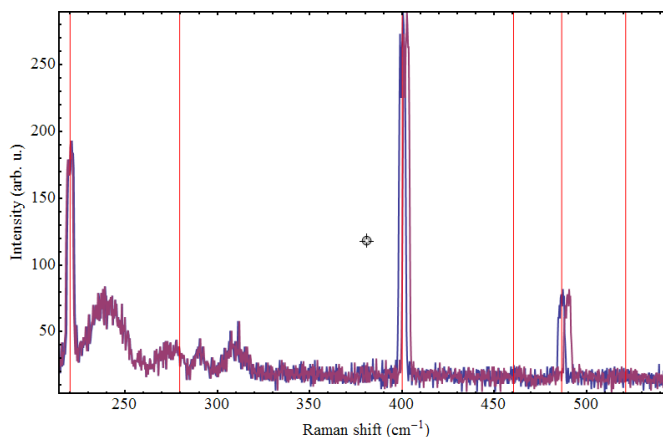
The procedure for reproducing the original spectrum now does not differ from one taken by a mixed gas laser. So at first, after loading the spectrum of the measured calibration lamp lines, the correct central pixel ($p=0$) has to be found. As mentioned above, not all measurements have to be taken with all available pixels of the detector (depending on the spectrometer software alignment). It should now be easy to reproduce the recorded spectrum by adjusting the focal length. This varies dispersion of the calculated spectrum, which should make it possible for the two spectra to overlap.

If the spectrometer is now moved a negligible Raman-shift error in a low shift (RBM)-region (central shift at $\sim 250\text{ cm}^{-1}$) is assumed. Then the wavelength can be adjusted in order to move the calibration lamp line positions from the calibration lamp datafile. If these lines overlap with the measured lamp lines, the correct wavelength should be found. This corrects the dispersion compared to the original spectrum, depending on the extend of the wavelength correction. In case the dispersion is not displayed correctly, the focal length can be readjusted. However, this last step should not be required for

NR-measurements. A significant error in dispersion could indicate a non-negligible error in Raman -shift in the RBM region.

For higher Raman-Shift regions (central shift $>500 \text{ cm}^{-1}$) the Raman shift error can be corrected by adjusting the reflection angle β , just as for measurements with gas lasers.

Figure 4.7: The original (purple) and the corrected (blue) Raman-spectrum is shown for a measurement with the Dye-Laser. The wavelength was significantly corrected from 577.5 to 580.668 nm, which results in a well-observable change in dispersion. F_{pre} and F_{post} were both set at 577.8 mm.



HR mode (Dilor XY)

For HR-measurements with a dye laser it is not recommendable to neglect the Raman-shift error in the low-shift region, as a higher accuracy in absolute wavenumbers may be required here. Even if the pre measurement calibration is performed very accurately, it is likely that the Raman-shift error becomes non-negligible after moving the spectrometer a few times (for HR-measurements). This makes it necessary to find a calibration lamp line in the spectral window of the laser line in order to find the correct laser wavelength. Due to the smaller spectral window it may be harder to find a gas line. Luckily, the spectral window can be enlarged by switching to NR mode of the Dilor XY spectrometer. As the spectrometer is not moved by doing this, a correct calibration can be performed. However, the accuracy of the calibration does not reach the same level as if the lines were measured in HR mode.

4.5 Summary of chapter 4

The simple model of the dispersion of light by a single grating provides a simple and reliable calibration after the measurement, providing the laser energy (or wavelength) is known with sufficient accuracy (e.g. noble gas laser). Then, an accurate pre measurement calibration to readjust spectrometer position with the detected position is in many cases not necessary anymore.

In case of the Dilor XY Raman spectrometer this is also true if more than one grating is involved in the diffraction process (HR-mode). However, for optimal accuracy the dispersion may have to be readjusted via two or more calibration lamp lines by varying the focal length. As the spectral window is very small in HR mode of the Dilor XY,

it is very important to have sufficient number of spectral positions of noble gas lines accurately saved. If only one spectral line is available within a spectral window, this can lead to a non-negligible error of the dispersion.

Providing a calibration with multiple symmetric lamp lines, the maximum accuracy of the Raman scale exceeds slightly its resolution (wavenumber-change per pixel see table 4.1). For the Dilor XY Raman Spectrometer, a maximum Raman scale accuracy of $\delta\omega \sim \pm 0.15/0.05 \text{ cm}^{-1}$ in NR/HR mode can be reached if the laser energy is known.

If a dye laser is used, the displayed zero position has to be accurately positioned in the center of the laser beam Lorentzian and a lamp line has to be measured here in order to correct the error in absolute position. If the latter was not performed, the spectrometer can be moved a bit to a low-shift region and measure the gas lines here. An accurate pre-measurement calibration is a requisite for this to obtain a similar level of accuracy. In this case, the error of the difference between laser position and RBM position is assumed to be zero. If this assumption is justified, an accurate value for the laser excitation wavelength can be found again, which also results in an accurate dispersion.

5 Raman Analysis of bundling and doping effects

5.1 Sample thickness

5.1.1 Radial breathing mode

In order to test a possible RBM-peak shift through CNT-density two CVD-grown samples with 0 % concentration of Acetonitrile (Nitrogen feedstock) were measured, where each of them showed a different thickness due to a different deposition time (1 minute versus 7 minutes). As the production process is apart from that the same, one might suggest there should not be a different diameter distribution. However, there could very well be an influence of larger deposition times on the formation process of CNTs and therefore also on the diameter distribution.

This could have impact on tube arrangements. A slight RBM-frequency shift of a specific peak for varying sample film thickness would indicate a change in CNT density on the nanoscale. For instance, a possible idea is that the array of vertically aligned tubes is modified for increasing film thickness, which may result in different intertube-interactions, as well as in additional chiralities.

A modified RBM-peak position by tube-tube VdW- interaction (compared to a interaction-free RBM-vibration) means a wavenumber blueshift, as the interaction results in a stiffening of the vibration coupling constant (see equ. 2.6). A blue- or redshift for increasing sample thickness now is the result of an increased or decreased (average) tube-tube interaction.

Also an effect on the FWHM (linewidth) of the peaks might be observable. The width is determined by the phonon population lifetimes, which are influenced by environmental perturbations (for instance, tube-arrangements like bundles, defects) [14, 38, 52].

Indeed we can observe a shift for different film thickness comparing the peaks at 205 cm^{-1} or even better at 240 cm^{-1} and 260 cm^{-1} in figure 5.1. The red line corresponds to the thick sample, therefore we observe here a slight loss in the RBM energy. There also is a slight change of the shape of the peaks at 240 and 260 cm^{-1} . Therefore, it seems not all nanotubes of a specific chirality are affected the same way of this density effect, since there are no other tubes geometrically possible in this region.

Similar observations were made for multiple other SWNT peaks at different laser excitation energies.

This suggests a decrease in tube-tube density for higher positioned layers of the sample, as the coupling constant is lowered for decreasing RBM frequency.

Surprisingly we observe high intensity narrow peaks for the higher density sample in fig

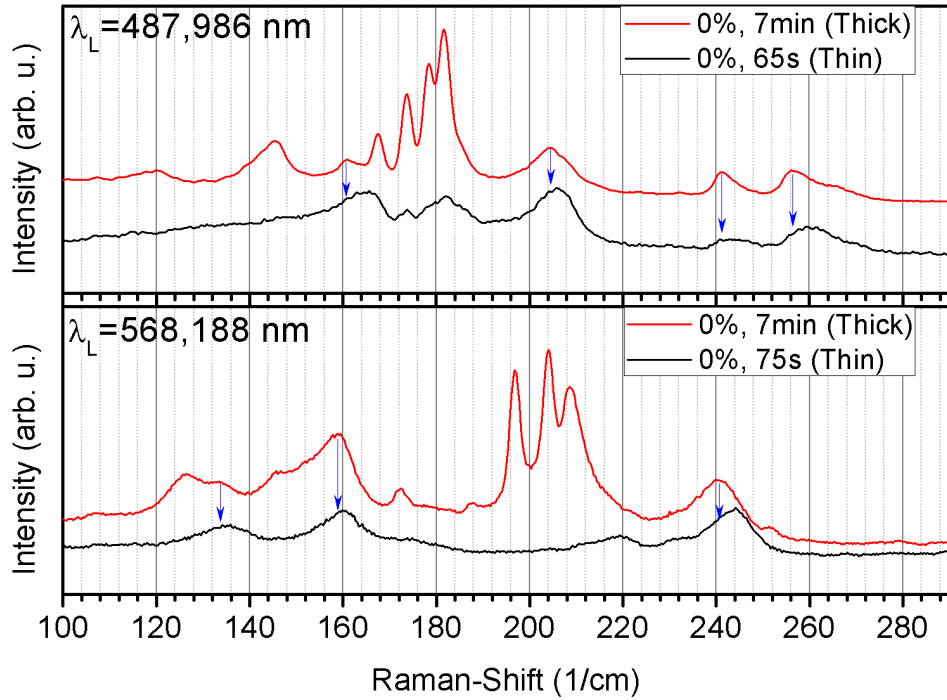


Figure 5.1: RBM modes of two 0% samples with different density measured in normal resolution mode at a excitation-laser wavelength of 487.986 and 568.188 nm. A blueshift of ω_{RBM} is observable for multiple peaks of for the thinner sample. The narrow and intense peaks of the thick sample are discussed in more detail in chapter 6.

5.1. As these peaks show a very strong increase in intensity (relative to the other peaks) for the thick sample, the presence of Double-Wall-CNTs is very likely. The increase in intensity together with the narrow FWHMs and the typical DWNT-cluster lineshape strongly support this assumption. This topic is analysed in this work later with more detail.

5.1.2 G'-line

With respect to the variety of applications and usefulness of the calibration method a possible environmental influence on the G'-Line is discussed. Analogous to the influence of the deposition/reaction time (sample thickness, and nanotube array arrangement) on the Radial Breathing Mode, there is a similar effect on the G'- Raman feature conceivable. Doping effects are considered later, only pure ethanol-based samples are used here. As this double resonance process includes 2 phonons (iTO near K-point in Brillouin-zone), a modification of the iTO mode is doubled and should favour the visibility. However, bundling effects on the Raman frequency on this mode have far smaller extend than on

the Radial Breathing Mode.

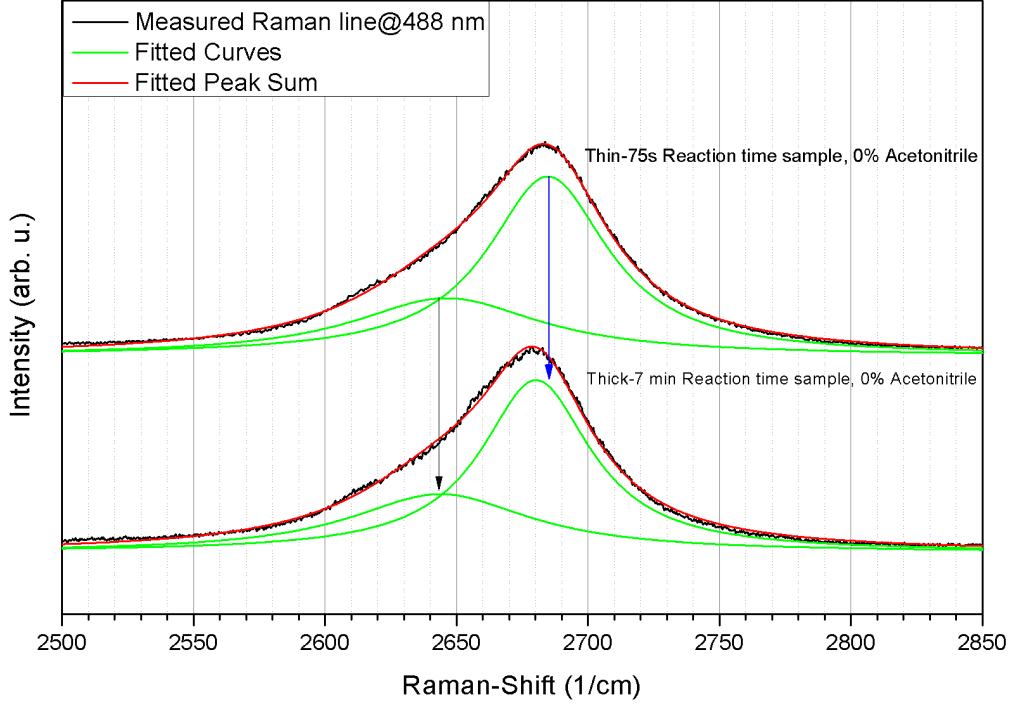


Figure 5.2: G'-Lines and their corresponding Lorentzian fits are shown for the thick and thin 0%-samples, respectively, for a excitation wavelength of 488 nm. A slight shift in frequency of $\sim 4 \text{ cm}^{-1}$ for the more intense higher frequency feature is detectable. Due to the accurate post measurement calibration, an error due to experimental variation can be ruled out.

Figure 5.2 shows a good reproduction of the G'-lineshape by fitting two Lorentzian Curves. This splitting can be most probably related to curvature effects ([50]). Additional not observable split components are possible, although not many very small diameter nanotubes are observed in the RBM-region (see figure 6.1). An influence of the sample thickness is much better observable for the major high intensity split component of this mode. Although the observed redshift for the thick sample of $\sim 4 \text{ cm}^{-1}$ (blue arrows in fig. 5.2) is very small, an influence by tube-bundling should be still possible. Measurements by Berciaud et al. ([5]) show a blueshift of the G' mode for applied pressure. Therefore, it is very plausible that a change of the arrangement of the nanotube array causes a lowering of bundling-effects and induces a redshift (similar to RBM features) for the thicker sample.

A simultaneously reduced FWHM would support this assumption, as lowered tube-bundling usually goes along with a prolongation of the phonon population lifetime and subsequently with a narrowing of the linewidth. Indeed, such a slight narrowing in linewidth is observable by the fitted Lorentzian curves (55 to 50 cm^{-1} , clearly exceeding statistical fit errors). The rather big linewidths are not surprising, as the sample contains

very heterogeneous carbon material. However, the lower overall intensity of the thick-sample spectrum (lower panel) leads to a lower elastic photon-scattering (spectrometer response), which also narrows the FWHM. This can not explain the narrowing completely, though.

Considering the spectrometer response and the fact that *two* iTO K-point phonons are involved in the scattering process, it can be seen that these phonons are much less sensitive to bundling effects than RBM-phonons. Figure 5.1 shows directly the RBM lines of the tubes in resonance. The RBM peaks at ~ 205 , 245 and 260 cm^{-1} show a redshift of roughly 4 cm^{-1} . This is roughly suggesting a lower sensitivity of the iTO K-point phonon to tube-bundling effects of a factor of 2 compared to the RBM-phonon (Γ -point). One has to keep in mind that this only applies for very low pressure or bundling effects (depends mostly on array arrangement and diameters).

The presence of strong DWNT-resonances (see fig. 5.1) of the thicker sample does not seem to have significant impact on the G'-band.

5.1.3 D and G-Line region

The D/G intensity ratio is generally a good measure for the quality of produced nanotubes. Therefore, this quantity is now used to determine the influence of the sample thickness on the overall tube quality of the sample.

The thickness-impact on the Raman-peak position for the D-mode peak has already been investigated by the G'-mode, as the same iTO K-point phonons are involved in the scattering process. As expected, the blueshift for the thicker sample is halved for the D-mode ($\sim 2 \text{ cm}^{-1}$ within resolution power) compared to the G'-mode (only one phonon involved).

For 488 nm excitation energy, where mainly semiconducting tubes are in resonance, the G-modes (LO and iTO, both Γ -point phonons) shows no variation in Raman shift position.

For 568 nm excitation energy, there is a BWF lineshape observable, which is typical for metallic tubes in resonance. There is an impact on the lower G-Line feature observable, which probably refers to the metallic LO phonon branch. The high intensity semiconducting LO-phonon branch is not influenced again.

The main feature of figure 5.3 is the reduction of the D/G ratio for the thick sample at both excitation energies. This has to be interpreted in context with the formation of high intensity-DWNT cluster lineshape in figure 4.2 for the thicker sample. The reduction of the D/G ratio supports the assumption of the increasing share of high quality inner tubes in the sample. This reduction is more significant for the 568 nm spectra (left panel), where a closer look reveals a higher intensity of the lower -frequency component of the D-mode.

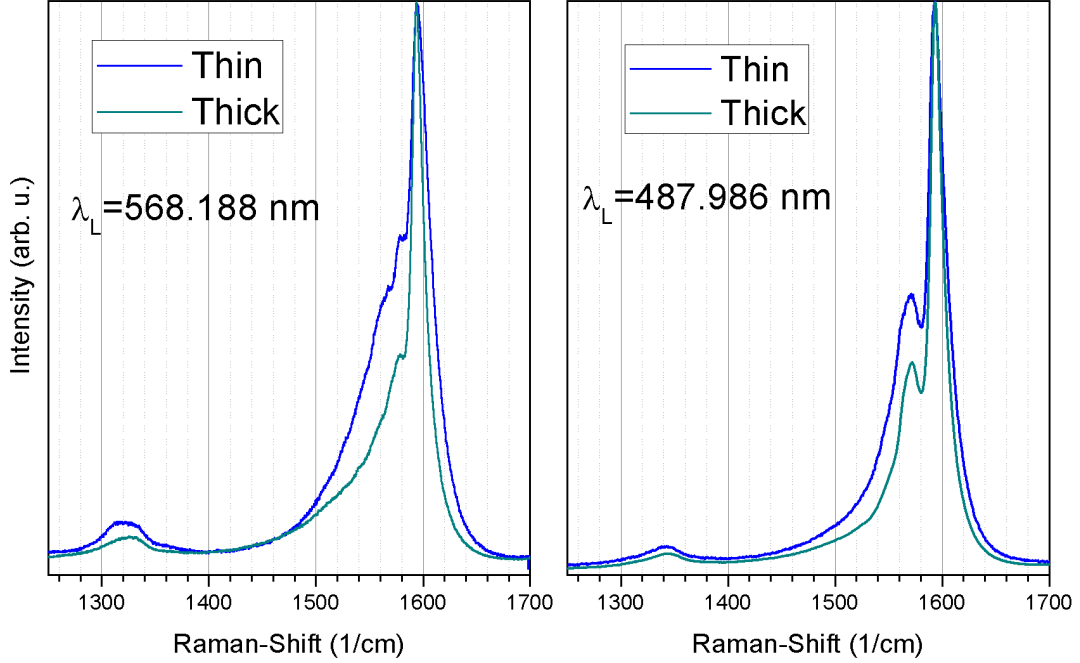


Figure 5.3: The comparison between the D and G mode for varying thickness of the carbon material film shows a clear reduction of the D-peak height for the thick sample. Both samples were produced without any N_2 -concentration in the feedstock. The decrease in intensity reflects an increase of the high quality inner tube share.

5.2 Nitrogen doping effects

5.2.1 Radial Breathing Mode

Previous reports claim a correlation between a decrease of mean diameter and the concentration of the incorporated nitrogen. Furthermore, it is reported that this concentration (and hence the diameter decrease effect) gets saturated by using 1 % acetonitrile in the feedstock. Therefore, any nitrogen effects should be fully featured in the 3 % acetonitrile sample. Figure 5.4 shows 2 pure ethanol produced and 2 Nitrogen doped samples, respectively, with the additional information of their deposition time.

Subsequently, this figure features 3 effects, where 2 of them have been already mentioned: These are the modification of the Raman shift position and the growth of DWNT-clusters (sample thickness, vertical tube array arrangement). The third feature is the increased share of smaller diameter tubes with increasing acetonitrile concentration in the feedstock, which is indicated by the arrows in fig. 5.4. This can be compared to ref. [50], where the same effect is demonstrated based on two other RBM peaks at a laser wavelength of 633 nm. For the two thicker samples (0 and 5 %), several additional RBM-spectra at wavelengths down to 488 nm are presented in the next chapter. This

allows to test the diameter decreasing effect by Nitrogen for different tubes in resonance (see fig. 6.1, 6.3).

However, the measurements at different excitation energies only suggest an influence of Nitrogen for low Raman-shift peaks (big diameter tubes). There was no influence of nitrogen for RBM features above $\sim 170 \text{ cm}^{-1}$ detectable. This is discussed based on a spectrum of the thick samples at 514 nm laser excitation wavelength (see fig. 5.5), but is already observable in fig. 5.4.

As mentioned above, fig. 5.4 also shows the growth of DWNT-clusters (later referred as cluster (10,7)), as the 3% sample with 3 min deposition time shows a significantly lower relative intensity and therefore a lower share of high quality inner tubes compared to the 7 min samples. The growth process is discussed later in more detail based on a different cluster (fig. 6.7).

In order to get a better quantification of the intensities, each RBM-spectrum is normalized to the corresponding intensity of the main semiconducting LO G-Line feature. Assuming the number of resonant (non-metallic) carbon material is proportional to the number of all resonant nanotubes, this normalisation is justified if the laser excitation wavelength is kept constant. Although this proportionality may not always be applicable (e.g. due to the preference of metallic inner-tube growth), this normalisation softens the systematic error of the highly sensitive experimental intensity- error. This normalization has been performed in several figures, as in fig 5.4. The 3% sample in fig. 5.4 additionally

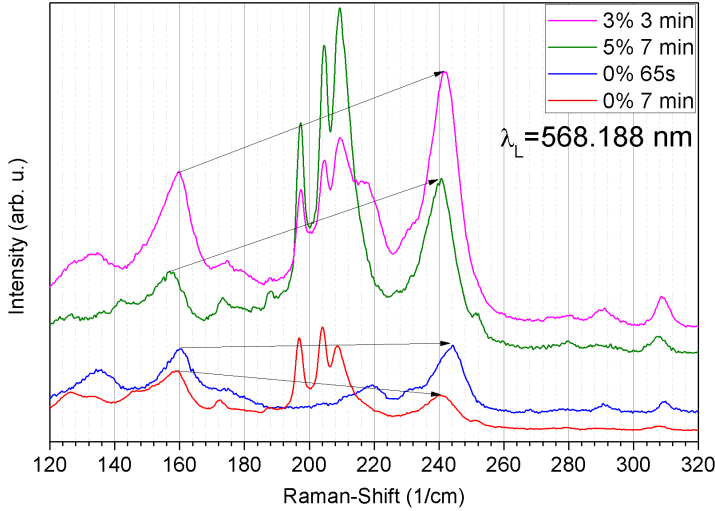


Figure 5.4: RBM modes of samples with feedstock-concentrations of 0%, 3% and 5% in normal resolution. The arrows indicate a possible change in mean diameter for different doping levels and film layer thickness.

represents an intermediate step regarding deposition/reaction time (3 minutes) or film thickness, respectively.

The modification of the RBM peak position is clearly visible again. For instance, the peak at $\sim 240 \text{ cm}^{-1}$ is exactly positioned between the thin 65s and the two thick 7 min -samples. The same effect can be observed for multiple other SWNT peaks with different magnitude for every individual peak (tube diameter).

The narrow inner tube split components do not exhibit a shift of the RBM peak position

among the two 7 min -samples and the 3 min -sample. This seems to underline the protected environment of the inner tubes provided by the outer tubes. Alternatively, this can reflect the insensibility of DWNT counter-phase oscillations to external perturbations (see section 2.4.1).

However, a (blue-) shift of inner tube split components is still thinkable for early stage grown DWNT: An increased environmental pressure on the outer tubes may slightly reduce their mean diameter and subsequently enhance the coupling force constant between inner and outer tube. Applying the serial coupled oscillator model to inner-outer tube RBM-oscillations, the total force constant of the oscillation is then also increased (equ. 2.6). Such an influence on inner tube resonances might be observable in later a discussion of a different DWNT-cluster growth (fig. 6.7, thin sample).

Figure 5.5: RBM modes of 2 thick samples (7 minutes deposition time) of 0% and 5% Acetonitrile concentration measured at 514 nm. The Raman profile changes significantly below 170 cm^{-1} . Additionally the small diameter tube quantity (peak-intensity) seems to be higher for the nitrogen doped sample.

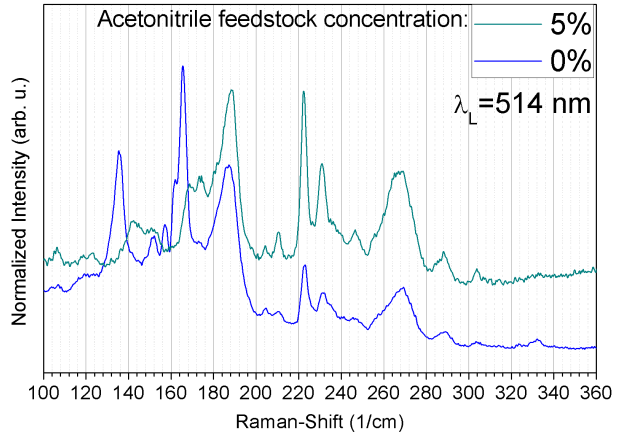


Figure 5.5 demonstrates a possible effect of diameter decrease again, as there is no artificial offset between the distinct spectra (as in figure 5.4). They are also normalized with the height of their corresponding main (LO) G-Line peak. The figure shows that the signal background increases significantly for the 5 %-sample in comparison to the 0% sample spectrum. As expected, there are no (slight) shifts for any of the observed RBM-peaks visible, as the sample thickness (deposition time) is the same for both samples.

All RBM-features above 170 cm^{-1} are present in both spectra, only the intensities are varying. Similar to the background, high Raman-shift features (above 200 cm^{-1}) show a higher intensity for the 5 %-sample. However, below 170 cm^{-1} there are some peaks present, which cannot be found for the 5% sample. This may suggest a large influence of Nitrogen for the formation of large diameter tubes.

5.2.2 G-band

Previous reports suggested a small blueshift for some G-band features at low dopant concentrations (n- or p-type doping, e.g. ref. [13, 39]). As the investigated samples features only low doping levels (~ 1 % N-incorporation, see ref. [50]), only very small modifications in Raman shift position are expected through doping effects. Therefore, a very accurate post measurement calibration is necessary to quantify small Raman shifts

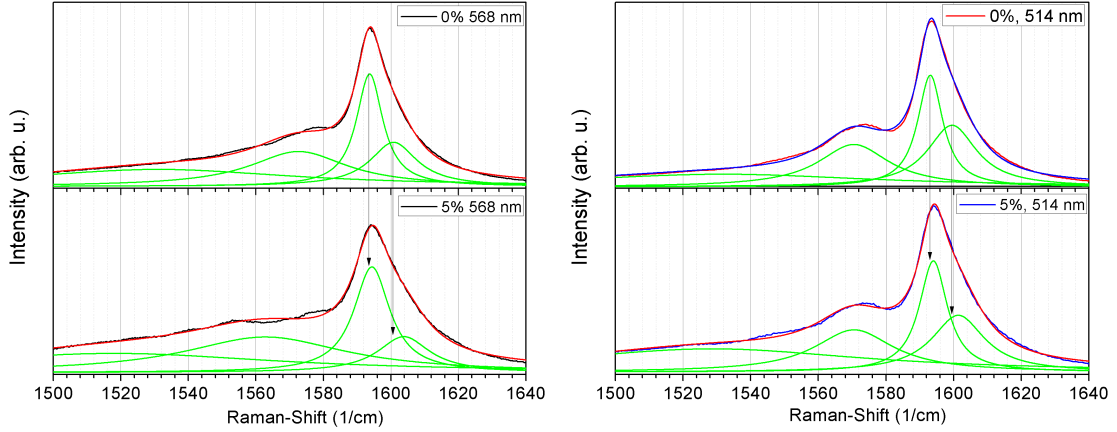


Figure 5.6: Despite the low doping level, there are small effects on the G-Band features observable. However, there are differences between the two excitation energies. For larger laser wavelengths (568 nm) the blueshift is slightly increased, which is in accordance with ref. [39]

below 1 cm^{-1} . Indeed, figure 5.6 reveals such a blueshift for the 2 highest shift G-band components (at ~ 1593 and 1600 cm^{-1} , respectively), as indicated by the arrows. All spectra were fitted with four Lorentzians. The high intensity main G band component originates from $A^{LO}(S)$ modes and the upshifted component probably from E_2^{LO} or E_1^{TO} modes. Curvature effects can be excluded as origin for splitting, as the vast majority of the tubes have diameter above 1 nm (see RBM spectra).

Despite the smallness of the effect, frequency shifts of $\sim 1 \text{ cm}^{-1}$ can be confidently quantified for the two $A^{LO}(S)$ components at both laser wavelengths. The higher shift components exhibit clearly larger shifts: At 568 nm the higher shift component exhibits a blueshift of 3 cm^{-1} , whereas at 514 nm the blueshift is below $\sim 2 \text{ cm}^{-1}$. Both split components exhibit slightly larger frequencies (below 1 cm^{-1}) at 568 nm.

At 514 nm a G-band component at 1570 cm^{-1} (A^{TO}) can be observed, which shows no modification in Raman frequency. At 568 nm a BWF-lineshape is dominating, which is slightly increasing for the n-doped sample, as expected.

5.2.3 G'-line

The presence of Nitrogen in the feedstock results in negatively charged defects in carbon nanotubes. Previous reports suggest a local renormalization of the electron and K-point phonon energies near these defects ([21]). In our case Nitrogen atoms represent these impurities, of course. This represents another application for a reliable post-measurement calibration, as this effect results in very subtle changes in Raman peak position at very high Raman shifts ($\sim 2600 \text{ cm}^{-1}$). A reliable calibration makes two different samples from different measurements more confidently comparable in order to quantify small Raman-shift related physical effects.

Another Raman-position modifying effect of the G'-Line important to be noted is the tube curvature (diameter). A decreasing diameter causes a phonon energy decrease and

an increase of the electron-phonon coupling, as studied in [30]. This dependence has been investigated through observing the slightly different G'-Line-dispersions of inner (smaller) and outer (larger) diameter of peapod-grown DWCNTs. In our samples there are not that many small-diameter nanotubes as expected from most CVD-grown nanotube forests. Nevertheless, a observable splitting of the G'-feature into two components can be expected of such a heterogeneous type of sample. For nanotubes with diameter above 1 nm the G'-Line roughly keeps its Raman-shift position, according to the study previously mentioned. However, there are also some tubes in our samples present that fall below this limit (above 270 cm^{-1} RBM shift, which is assigned to tubes with diameter less than 0.85 nm). This diameter-limit, where curvature effects cannot be neglected, can be depicted in Figure 10 in ref. [30].

Thus, these two effects have to be considered for analysing the existence of two split components (ignoring the sample thickness related described above). In ref. [50] the conclusion (same samples) is drawn that the curvature effect is the dominating and determining force for the G'-Line splitting. This conclusion is related to the fact that XPS-measurements revealed only 1.2 at. % substitutional incorporated-Nitrogen in pure Acetonitrile grown samples. However, detailed RBM studies in this work and the above mentioned diameter-limit for non-negligible impact on K-point phonons do not support the curvature effect as unique origin for the observed splitting.

The influence of Nitrogen on the G'-Line has been measured for the three samples, one thick sample with 5 % Acetonitrile in feedstock (7 minutes deposition time) and two thin samples with 0 and 3 % (75 seconds deposition time).

Figure 5.7 demonstrates the growth of the lower split components with increasing nitrogen incorporation. The pure ethanol produced sample spectra also features a clearly visible split component. This strongly points towards a curvature influenced phonon energy. Therefore, it seems plausible that the increase of this component in the two lower panels originates from an increase of the small-diameter tube share in the sample. Especially, considering the increase of electron-phonon coupling for small diameter tubes, this assumption does seem legit. However, figures 5.4 and 5.5 already indicate only a minor influence of the N-doping on the formation of small-diameter tubes ($d < 1 \text{ nm}$). A comparison of figures 6.1 and 6.3, whose spectra cover a large range of laser excitation energies (2.18 - 2.56 eV), confirms this impression. The observed influence of the doping on the large diameter tubes (discussed in next section) does not justify the splitting range of $30 - 40 \text{ cm}^{-1}$ depicted in figures 5.7 and 5.2.

Both effects potentially responsible for the G'-Line splitting discussed in references [21] and [30] result in a very similar splitting range. This is also holds if the linear dispersion of the G'- mode for different excitation energies is taken into account, which was measured in both articles mentioned above. Therefore, the most intuitive explanation is a strong overlap of both effects, which results into the emergence and growth of the lower split components (blue lines in fig. 5.7). As the dispersion of this split component is also very similar for both effects, additional laser energies probably will not reveal a third G' - component.

The potential influence of Nitrogen on mean-diameters is already saturated for a small concentration of Acetonitrile in the feedstock ($< 1 \%$, as reported in [50]). This fact

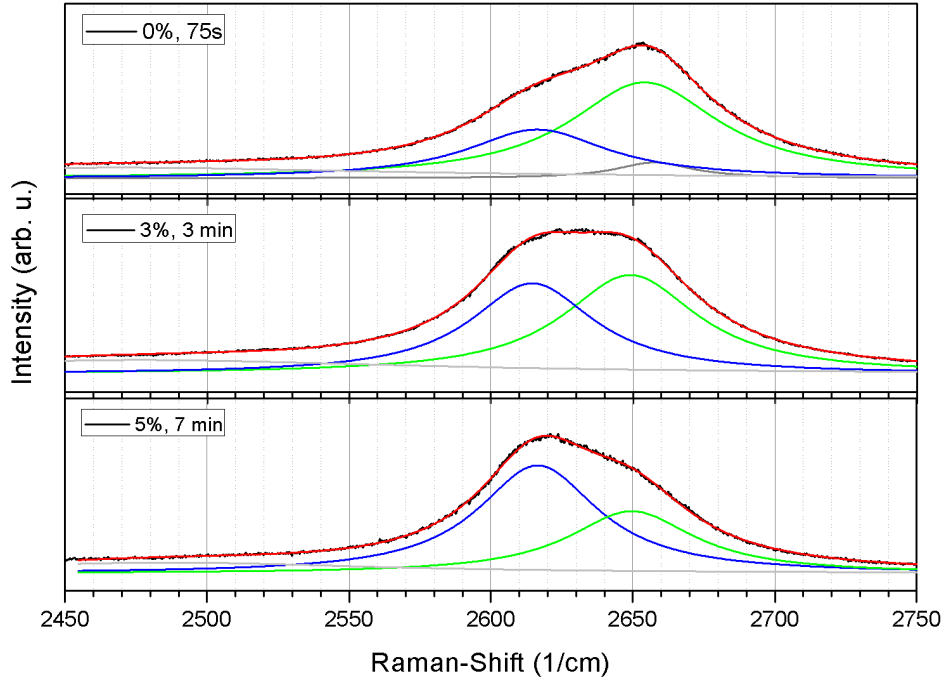


Figure 5.7: G'-Line of samples with three different concentrations of acetonitrile in the feedstock at 568 nm laser excitation energy. The substitutional incorporated Nitrogen clearly has impact on the intensity ratio of the two split components (blue and green lines). As the pure ethanol produced sample also clearly featured a lower split component, a clear curvature related splitting is observed here. However, the increase of the lower split component in the two lower panels may be related to a phonon energy decrease based on negatively charged defect sites

strongly favours a major influence of substitutional Nitrogen rather than curvature on the lower split components (blue lines). This conclusion is drawn based on the two lower panels (3 and 5 % sample) in fig. 5.7. The intensity-increase of the blue line in the lowest panel indicates a strong dependence on the concentration of Acetonitrile in the feedstock, despite the saturation of the smaller mean-diameter at already 2 % of Acetonitrile, as reported. A comparison of RBM spectra of the 3 and 5 % samples confirm a not changing mean diameter (e. g., fig. 5.4).

However, a decrease of the mean diameter may still contribute to this effect, especially if considering that XPS-measurement revealed a maximum (saturated) nitrogen content of only ~ 1.2 at.% in the samples.

5.3 Summary of chapter 5

The investigated samples seem to reveal consistent phonon energy influencing effects for various phonon modes. The extend of the influence varies for each individual phonon

band.

Different sample layer thickness seems to have clear impact on the vibrational properties of the no-flow CVD produced samples, especially for RBM vibrations. Here clear Raman redshifts up to 4 cm^{-1} were observed, which indicates a significant change of tube environment of higher positioned sample film layers. The RBM is very sensitive to environmental pressure, despite being a low-energy Raman feature. Higher energy phonon modes are significantly more insensitive to this. For instance, there could not be an impact on the G-band frequencies for varying sample thickness observed. In case of the G'-band (two phonon scattering process), there could be a slight shift up to $\sim 3\text{ cm}^{-1}$ confidently quantified, which may be correlated to a change in tube bundle arrangements.

Substitutional nitrogen clearly has larger impact on the higher energy phonon modes. Although the observed Raman-shift change was very little for the G-band (often less than 1 cm^{-1}), it is still detectable due to an precise post-measurement calibration. The nitrogen concentration in the samples was rather low (see ref. [50]), which results always in a blueshift for the G-band according to a simple model in ref. [39]. It describes the "G-mode" simply as two oscillating carbon atoms, whose vibration is influenced by distant charged dopants. This simple model can in principle explain the observed blueshift, despite the low concentration of nitrogen atoms. A shift has been observed at two (higher shift) components of the G-band at ~ 1595 and 1600 cm^{-1} , where the origin of the latter could not be unequivocally identified.

In contrast to the G band, the G'-band is softened for n-type doping and therefore the corresponding Raman peaks exhibit a redshift (according to ref. [21]). Indeed, increasing the concentration of the nitrogen containing feedstock increases the intensity of the G' split component with lower Raman frequency. Surprisingly, the purely ethanol based sample also features a lower split component, as revealed by deconvolution with Lorentzians. This component may stem from curvature effects, as the corresponding RBM spectra reveal tubes above 300 cm^{-1} in resonance.

The RBM-frequencies are not influenced by the n-type doping, but according to ref. [50] the mean diameter of the sample distribution can be lowered. As only intensity ratios can be considered in this work, this could not be explicitly confirmed. However, there could be a influence on big diameter tubes, as the RBM profile changes dramatically for the low shift region below $\sim 170\text{ cm}^{-1}$.

6 Detailed Raman analysis of DWNT RBM-clusters

The detailed RBM analysis were performed for the 2 thick CVD - grown samples, one N₂-doped (5 % Acetonitrile), the other not, respectively. The reason that only these samples were chosen is on the one hand a strong Raman signal, which promotes reliable Raman spectra, on the other hand these samples show interesting RBM - lineshapes, which could correspond to Double wall - CNTs. Besides DWCNTs, other explanations for DWCNT-like behaviour are possible.

DWCNTs would be very interesting indeed, as the parameters of the production process did not intend to produce DWNTs. The environmental conditions could favour the growth of certain types of inner-outer tube pairs. The quantity of DWNT in relation to other tube material seems proportional to the deposition time in the reaction chamber.

The origin and features of the DWNT splitting clusters are already discussed in chapter 2.4. Especially the samples with a thick carbon material film feature narrow splitting clusters typical for DWNTs, as plenty of figures (4.5, 5.1, 5.4) in the previous chapters already have shown.

It should be pointed out that the focus of this analysis is not the lifetime of the excited electron and phonon states, which influences the intensity and the linewidth of the observed Raman signals. As mentioned in chapter 2.4, a outer tube can favour the growth of perfect nanotubes with almost no defects ([29]). This is the most influential factor for the lifetime of the excited states and the phonons and therefore also for the intensity and linewidth. The Raman intensities are also affected by a number of experiment dependent factors such as the surface morphology of the samples. As a result of this, allegations made through peak intensities have to be enjoyed with caution. However, the linewidth and position of the Raman-features still can deliver very interesting information about the phonon lifetimes and hence the environmental conditions of the RBM vibrations.

If the signal of the inner tubes is low and broad, it is still possible to assign it to a DWNT vibration. This can be observable through fitting if there are more than the geometrically allowed peaks visible (despite overlapping). In case the peaks should correspond to SWCNTs with different diameter, there should be a fitting geometrically possible group of tubes with only slightly differing diameter. However, also vast changes in changes in energy transitions cannot be singled out without other spectroscopic methods.

As the splitting-width can be very large for inner tubes, the assignment of the splitting features can be difficult. In contrast to the slight blue-shift of RBM frequencies through decreasing sample thickness in previous chapters, we now deal with much stronger in-

interaction effects (coupled oscillators). Therefore the splitting effect now exceeds a small phonon energy loss caused by a weak-interaction nanotube bundling. Additionally, the observed higher energy counter-phase resonances should mostly be insensitive to external influences and provide well-defined vibrational energies (see chapter 2.4.1).

Nevertheless, the possibility of bundling effects have to be taken into account. As described in the previous chapter, bundles can show a similar effect of an increase in RBM-vibration energy through VdW interaction energy. However, this requires a clean nanotube bundle register. Therefore the interaction effect cannot be evaluated with the same reliability as for inner-outer tube pairs.

For CVD-produced SWNT samples on a quartz substrate, good results were obtained ([2]) by choosing $A=217.8 \text{ cm}^{-1} \text{ nm}$ and $B=15.7 \text{ cm}^{-1}$ as fitting parameters. As the investigated samples in this work were produced the same way, these values might provide good results for observed SWNT peaks. Similar results for nanotube diameters are obtained by using $A=224 \text{ cm}^{-1} \text{ nm}$ and $B=14 \text{ cm}^{-1}$ ([38]). These values were derived explicitly for nanotube bundles and are providing slightly larger diameters about 0.2 \AA . However, this difference is negligible. A broad RBM peak which cannot be assigned to a SWNT chirality is under suspicion to originate from a DWNT vibration.

These two sets of parameters should provide an appropriate and sufficiently accurate assignment of diameters for the SWCNT- RBM resonances (linewidth $5\text{-}10 \text{ cm}^{-1}$) of the investigated samples. However, it could be interesting to consider the (experimental) parameters obtained for suspended SWCNT ([20]). As the nanotubes were suspended over slits here, environmental interaction effects were excluded. It might be possible that these (VdW-) interaction effects are also excluded for inner tubes in DWCNTs, provided that the wall-to-wall distance ΔR is large enough. Therefore it might be promising to look at the dependence of the inner-outer tube interaction energy on ΔR , as described in the previous section. According to equation 2.7, the second derivative of the interaction potential Φ plays a major role for the modification of the force constants. Previous results [51, 19] suggest a vanishing second derivative and subsequently a very linear potential $\Phi(\Delta R)$ for $\Delta R > 3.9 \text{ \AA}$. However, such large inter-wall distances might prevent a concentric arrangement of inner and outer tube.

Another interesting topic is the influence of the N-doping to the sample properties. The effect of Nitrogen to the growth of nanotubes can also be observed through an electronic microscope (SEM). It is investigated whether the diameter decrease effect or other RBM influencing effects are observed. A share of Acetonitrile in the feedstock above 5 % does not result in a higher concentration of incorporated N_2 , as reported (ref. [50]). The different feedstock may have impact on the growth on the DWNT-clusters in addition to the changes already discussed in chapter 5.2.

6.1 Experimental results

6.1.1 0 % sample measurements

Figure 6.1 shows the RBM excitation spectra with all wavelengths for the 0 % Acetonitrile sample. The measurements were performed with an Ar-Kr mixed gas laser and the

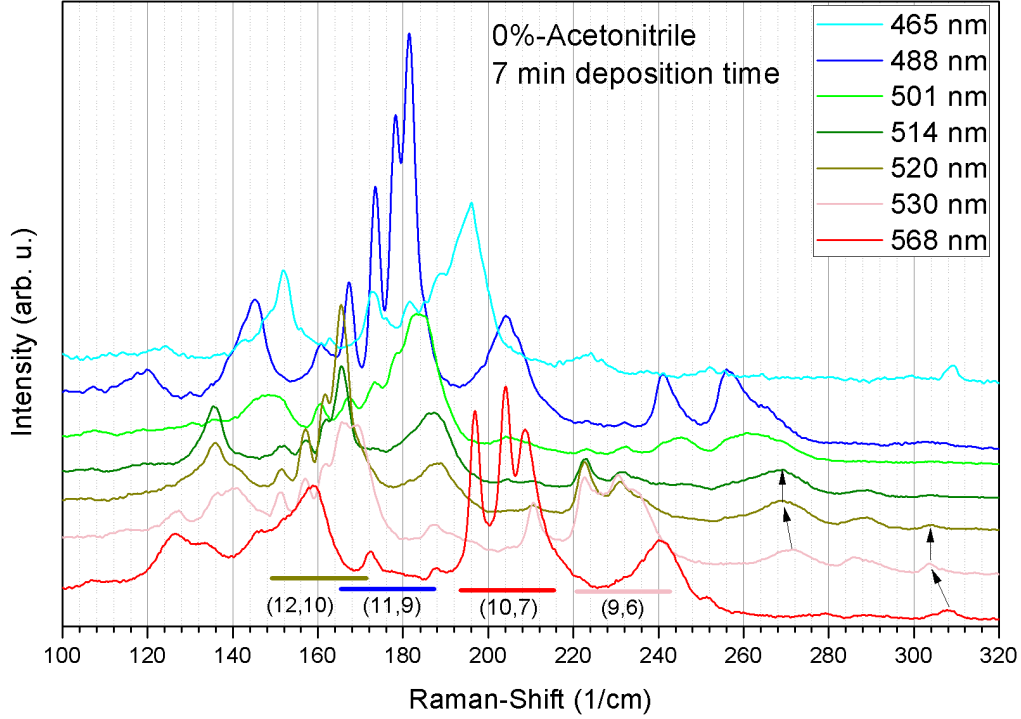


Figure 6.1: RBM peaks for different laser excitation energies for the 0 % acetonitrile sample with 7 minutes deposition time. The range and the inner tube chirality of the DWNT clusters are indicated at the bottom. Their color corresponds to the laser wavelength with maximum visibility.

DilorXY Raman spectrometer, as before. The laser excitation energy ranges from 2.18 to 2.56 eV, which covers a large range of nanotube diameters up to 2 nm. The potential nanotubes in resonance are represented by the overlapping shaded areas in the Kataura plot in figure 2.4 in section 2.1.2.

As indicated in previous chapters, certain high intensity and narrow RBM lines suggest a well-protected and defect-free environment for corresponding nanotubes and excited electron states. This features are typical for the presence of DWCNTs and cannot be overseen for both long deposition-time samples.

However, also lower intensity peaks may correspond to DWNTs, as one of the most important parameters for the RBM intensity is the quantity of resonant tubes. Therefore, observed changes of the vibrational properties due to inner-outer tube interaction can be a useful indication for DWNTs.

The investigated samples reveal strong populations of DWNTs only for larger diameter tubes above 1 nm. This is not an unusual observation for nanotubes with this type of production procedure (ref. [18, 53]). Our sample does not show sharp and narrow resonances in the spectral range of 240-400 cm^{-1} , which is the region mostly investigated for highly defect-free inner tubes (peapods and CVD grown).

High-shift RBM features and possible DWNT effects

Above 300 cm^{-1} we see small peaks, which originate from small diameter nanotubes ($< 0.8\text{ nm}$, Kataura plot). These are visible at lower excitation energies like 2.33 (530 nm) or 2.18 eV (568 nm) and can be assigned to semiconducting type 2 (S_{II}) $(6,5)$ nanotubes. This assignment through RBM-frequency is independent of the specific choice of A and B in equation 2.11, since there are no other geometrically allowed tubes within this region. We can observe a quite big shift (see arrows) of the peak from 568 nm to 530 nm to the left. The peak remains visible until $514\text{ nm (}=2.41\text{ eV)}$ holding the position. This is an strange observation, as these excitation energies should be too high (low) for the lower (higher) transition energies of such small-diameter tubes ($\sim 0.75\text{ nm}$). This may indicate a change in tube-tube interaction (shift) as well as a change in transition energy. However, it is hard to say if this shift is due to a inner-outer tube interaction of DWCNTs or other effects like SWCNT-bundles. The difference between isolated and nanotube bundles has been previously observed [38]. The increase of transition energy of $\sim 0.2\text{ eV}$ reported here would fit to the observations in figure 6.1. However, the RBM-frequency should be blue-shifted (up to 10 cm^{-1}), in contrast to the observed red-shift of 4 cm^{-1} . Subsequently the peaks at 304 cm^{-1} could refer to tubes which feel less interaction, but the broadened resonance profile (peak visible up to 514 nm) points toward bundles. Thus, the higher shift Raman feature (at 308 cm^{-1}) refers very likely to inner tubes. A narrower resonance profile would support this assumption. Dye-laser measurements performed around 568.188 nm laser excitation wavelength with similar produced bucky-paper samples confirmed the narrow resonance profile of same peak.

The slightly bigger diameter tubes visible ($268/288\text{ cm}^{-1}$, $(9,3)/(10,1)$, respectively) are metallic (M) tubes, which can be very well assigned by using the constants A,B for CVD-grown nanotube bundles in equation 2.11 ($A=217.8/224$ and $B=15.7/14$). These peak show a very broad resonance profile of $\sim 200\text{ meV}$, as they are visible from 530 (2.33 eV) to 501 nm (2.47 eV) . This is a strong indicator for the presence of nanotube bundles ([25]). Although these small diameter tubes can be assigned very confidently to their chiralities, a quantification within small Raman shift regions (around 2 cm^{-1}) of the peak position is unreliable if the reference point parameters come from literature.

However, such small shifts could still be quantified, if the reference-point (or -peak) comes from the same sample-spot, providing an exact calibration of all spectra. With this in mind a similar effect as for the $(6,5)$ tubes can be observed for the $(9,3)$ -peak at 268 cm^{-1} : At 530 nm laser wavelength there is a slight upshift of the peak from 268 (at $501\text{-}520\text{ nm}$) to 270 cm^{-1} visible. Therefore an upshift again comes along with a decrease of the energy-transition ($\Delta E \sim 100\text{ meV}$), even though to a lesser extend. The presence of inner tubes could be again a reason for this effect.

To an even smaller extend, this effect again seems to be observable for the peak at 230 cm^{-1} . Although overlapped, the resonance seems here very strong at 530 nm . In contrast to the previous peaks, the assignment to the tube chirality via zone-folding energy transitions and equ. 2.11 seems problematic for this peak. This clearly points towards strong interaction effects or DWNTs, possibly similar to the $(6,5)$ -peak. The

peaks at 230 and 236 cm^{-1} are likely to be part of a DWNT-splitting cluster and therefore stem from the same inner tube. These clusters are analysed in more detail in the following.

Despite the change of the Raman-Shift of only $\sim 1 \text{ cm}^{-1}$ is very small here and comes close to the resolution power of the spectrometer in NR-mode, this effect can be assigned confidently here, as it gets confirmed by an additional spectrum (fig. 6.3) and an accurate post-measurement calibration.

Large-diameter DWCNT splitting clusters

Figure 6.1 shows 4 evident clusters of strong and narrow resonances, which do not appear in the spectra for the thinner films, whose substrate was exposed a shorter time in the reaction chamber. For 2 of these clusters a clear resonance profile can be observed (cluster (9,6) at $\sim 220\text{-}240$ and cluster (12,10) at $\sim 150\text{-}180 \text{ cm}^{-1}$). The other two clusters (cluster (10,7) at $190\text{-}220 \text{ cm}^{-1}$ and (11,9) at $160\text{-}190 \text{ cm}^{-1}$, respectively) are visible at mostly one laser excitation energy each (the former at 568 nm (2.18 eV) and the latter at 488). However, cluster (11,9) is also weakly visible at 501 nm.

It can be seen that the resonance profile seems homogeneous for every peak in the respective cluster, for cluster (9,6), (12,10) and (11,9) this can be seen explicitly. For cluster (10,7) it can be seen that every peak is visible only at 568 nm. Exceptions of this principle may be a hint for distinct nanotube chiralities or a significant change in transition energies.

The homogeneous resonance profile indicates that it is very unlikely that the individual narrow peaks per cluster correspond to distinct nanotube-chiralities. This together with the fact that most linewidths of the observed peaks are very narrow (which is typical for DWNT-inner tube resonances) makes inner tube splitting the most plausible explanation for these observed features. Thus, every cluster should correspond to one specific inner tube type, similar to figure 2.8.

Of course, these presumptions and assignments have to be confirmed by structural analysis measurements.

As described in section 2.4.1, the presence of other tubes (bundles) or the outer tube wall results in a modification of the coupling constant of the corresponding RBM mode, as the RBM vibration can be described by a harmonic oscillator. In the same manner DWNTs can be described by coupled (-quantum) harmonic oscillator ([19, 12]). This modification usually means an increase of the coupling constant, as the second derivative of the tube-tube interaction potential should not get negative (always attractive force), even for large tube-tube distances. This means only an increase of the RBM frequency (blue-shift) is likely through this effect. However, as the detailed shape of the interaction potential is not fully understood yet, potential (slight) redshifts cannot be completely excluded.

The tube-tube interaction of SWCNT-bundles is more difficult to characterize, as there do not exist such arrangements like inner-outer tube pairs which make an accurate assignment of the peaks possible. Nevertheless, this effect has also been investigated ([25, 38]) by comparing bundled to individually dispersed nanotubes. Some studies confirmed that certain types of bundled tubes showed an increased RBM vibration energy (along with

modified transition energies). The main factor whether nanotube bundles exhibit this behaviour is determined by the arrangement of the nanobundle-register and its defects (see ref. [25]).

As described above, the typical features of nanotube bundles are broadened RBM-peaks, a broadened resonance profile and (most times) lowered energy transitions.

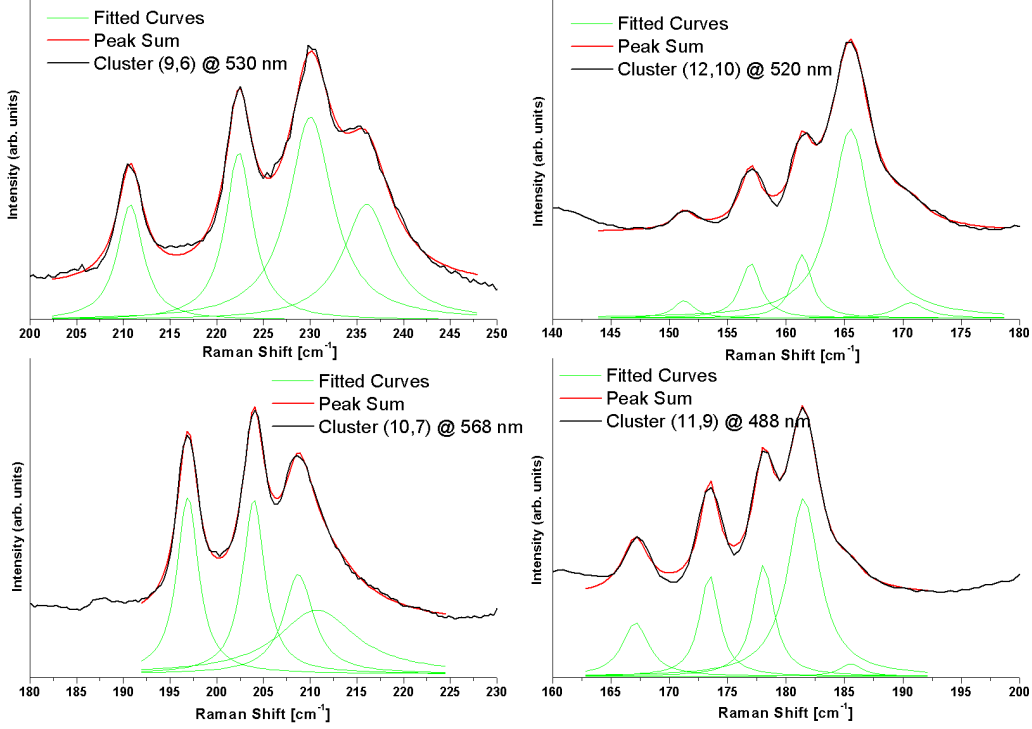


Figure 6.2: All clusters are reproduced by fitting Lorentzians for their corresponding spectra which feature the largest intensity. Except for cluster (9,6) (5 % acetonitrile sample, figure 6.3), all shown clusters originate from the 0 % acetonitrile sample (figure 6.3).

Cluster (9,6) (at 220-240 cm^{-1})

The sharp resonances around 220-240 cm^{-1} are the first promising candidates for large diameter inner-tube splitting (beginning with the smallest diameter tubes). They can be quite confidently be assigned to (9,6) nanotubes, as their transition energy $E_{11}^M = 2.376$ eV (nearly) matches the observed resonance profile (with the largest theoretical resonance at 520 nm). The peaks (at 222 and 230 cm^{-1}) are visible at every used excitation energy, except for 568 nm. This suggests a resonance profile with a width of $\Gamma \sim 50$ meV, as the peaks around 2.4 eV excitation energy are very small. This is not unusual for resonance profiles of inner tubes ([47]).

The RBM-features at ~ 230 cm^{-1} and 530 nm has a very strong background, which already indicates an upshifted broad SWNT-like peak. Deconvolution reveals a broad

resonance at $\sim 236 \text{ cm}^{-1}$. As the resonance profile for these two peaks does not make different types of tubes possible, an different environmental interactions are the only possible explanation here. The broad peak at 236 cm^{-1} could theoretically correspond nanotube bundles, but would require very strong bundling interactions. A strong tube-tube interaction (not necessarily through bundling) is suggested by the observed reduction of the transition energy, as the peak is not visible at higher excitation-energies (501, 488 nm) anymore.

It seems strange that the peak which refers to nanotube bundles should be more influenced by environmental effects than components of (potential) inner tube splitting at 230 and 222 cm^{-1} . Therefore it seems very plausible that the broad peak at 236 cm^{-1} corresponds to an additional (9,6)- inner tube split component. As this cluster is the one referring to the smallest tubes, the assignment is here the safest among all observed clusters.

The peak at 222 cm^{-1} can be accurately mapped to the (9,6) diameter ($d = 1.023 \text{ nm}$) by using the parameters $A=228$ and $B=0$ in equation 2.11 for clean suspended SWCNTs with no environmental influences ([20]). Thus these inner tube vibrations seem to be completely protected from the environment and are not influenced by the outer tube partner(s). This would require large interwall distances.

Cluster (12,10) (at $150\text{-}180 \text{ cm}^{-1}$)

This cluster features the biggest tubes exhibiting this effect, which makes the assignment more difficult as there are more geometrically allowed tubes possible. Nevertheless, the resonance profile of the tubes at this position can be most likely assigned to (12,10) nanotubes, which have a transition energy of $E_{33}^{II} = 2.379 \text{ eV}$. This value (derived through zone folding approach) matches exactly the resonance profile observed: The strong and (quite) narrow resonances are visible within a spectral window of $\sim 75 \text{ meV}$ (2.33 (530) - 2.41 (514) eV (nm)) with the strongest resonance at 520 nm (2.38 eV).

A closer look (through deconvolution) reveals again a broader bundle-like peak at high shift (right) side of the cluster. The peak position can be very well reproduced through the (14,7)-tube diameter by using the parameters A, B in equation 2.11 for bundled tubes. The resonance profile of this peak also supports this assumption, as it is only well visible at 530 nm and disappears completely for laser wavelengths below 514 nm . Analogous to other clusters ((10,7) and (11,9)), this peak can alternatively be assigned to an additional split component of the (12,10) inner tubes, along with a slight modification of the transition energy (and eventually electron-phonon coupling). For cluster (9,6) this is the only possibility to assign the broad peak, as tube bundles are geometrically not allowed here.

The resonance profile of cluster (12,10) is clearly moved towards higher energies (50-100 meV) compared to the broad resonance. The assignment of these peaks (at 151, 157, 161 and 165 cm^{-1}) to the splitting components of (12,10) inner tubes follows the pattern of other clusters, but bundled SWCNTs would also be geometrically possible (e.g. (13,9) or (15,7) by using A, B for nanotube bundles. However, the common resonance profile of these peaks strongly supports the assumption of (12,10) splitting components.

Analogical to all the other clusters, the peak position of the lowest Raman-feature (here at 151 cm^{-1}) can be very accurately reproduced by using A, B for suspended high-quality single-wall tubes and the zone-folding diameter $d_{(12,10)}=1.49\text{ nm}$ in equation 2.11.

As cluster (12,10) features more split components as the other clusters, the change of intensities from peak to peak can be well observed and may reflect the distribution of wall to wall distances. Therefore a formation of a inner-outer tube pair with sufficient large interwall distances for vanishing coupling constant may occur with the smallest probability, which is why the peak at 151 cm^{-1} has the smallest intensity compared to the others.

Cluster (10,7) (at $190\text{-}220\text{ cm}^{-1}$)

The next cluster of inner tube resonances referring to slightly bigger tube diameters is around 200 cm^{-1} at 2.18 eV excitation energy (568 nm). These even narrow and more intense peaks (compared to those of cluster (9,6)) stem clearly again from metallic tubes (E_{11}^M -transition). In fact there are four peaks visible, as at 210 cm^{-1} there are two peaks convoluted and the left one dominates at 568 nm . They show a similar behaviour like cluster (9,6): The resonance profile seems to be very narrow again, in which too high excitation energy spectra ($530, 520$ and 514 nm) still show tiny but visible peaks at the position of the strong resonances (196 and 204 cm^{-1}) at 568 nm .

However, there is an important difference to cluster (9,6): The right peak of the two convoluted peaks at 211 cm^{-1} still exhibits a strong resonance at the 530 nm spectrum. Obviously this is an exception of the presumption that all or no peaks are visible at a certain excitation wavelength. These observation can be explained by assigning the (deconvoluted) peak at 211 cm^{-1} to a different tube chirality than the other strong resonances at $210, 204$ and 196 cm^{-1} (568 nm): The position at 211 cm^{-1} can correspond to (11,5) nanotubes with a zone-folding transition energy of $E_{11}=2.29\text{ eV}$, which is likely to be lowered by $\sim 100\text{ meV}$ through bundeling effects ([25]). The observation of quite strong resonances at both spectra (568 (2.18) and 530 (2.33) nm (eV)) is indicating a broadened resonance profile ($\Gamma \sim 200\text{ meV}$). The peak also remains visible at even higher excitation energies, but with very low intensity. Additionally the Raman peak position can be mapped very accurately to the (11,5)-tube diameter by using constants A, B for nanotube bundles in equation 2.11.

The three strong and narrow peaks of cluster (10,7) should correspond to splitting components of (10,7)-inner tubes with a zone-folding energy transition of $E_{11}=2.15\text{ eV}$. This assignment leads to a very interesting analogy to cluster (9,6): The peak at the smallest Raman-shift position (at 196 cm^{-1} for cluster (10,7)) can be very accurately assigned to the corresponding inner-tube diameter by using again the constants $A=228$ and $B=0$ in equation 2.11 derived for suspended nanotubes. Subsequently the remaining peaks at 204 and 210 cm^{-1} refer to different interaction energies of the inner (10,7) tube.

As for cluster (12,10), the broad resonance can also be assigned to an additional inner tube split component. The absence of (11,5)-bundle resonances for thinner samples with lower deposition time supports this assumption.

Cluster (11,9) (at $\sim 160\text{-}190\text{ cm}^{-1}$)

Although the resonance profile of this cluster is not measured with the same numbers of corresponding excitation energies as for cluster (12,10), the chiralities can be very confidently assigned to (11,9)-tubes for the sharp resonances. As the resonance profile of the inner tubes should be very narrow again, the transition energy would have to be very close to the 488 nm (2.54 eV) spectrum, as the observed peaks are very intense at this energy. Indeed, this is the case for (11,9)-tubes ($E_{33}=2.56\text{ eV}$). The 501 nm as well as the 465 nm spectrum confirm a common resonance profile for all narrow peaks.

The use of equ. 2.11 offers again an accurate assignment of the zone folding diameter $d_{(11,9)}=1.35\text{ nm}$ to the observed RBM-peak position at $\sim 167\text{ cm}^{-1}$. This lowest observed peak-position can be reproduced very accurately again by using the constants $A=228$, $B=0$ of suspended SWCNTs ([20]).

The intensities of the peaks of this cluster show the same shape as the peaks of cluster (12,10). As before, this may reflect the distribution of inner-outer tube distances.

At the high-shift side of cluster (11,9) (at $\sim 184\text{ cm}^{-1}$) is again a small, broad peak with a broad resonance profile visible, which may refer to (13,6)-nanotube bundles. However, it is also very possible that this again refers to an additional inner tube split component, which corresponds to the lowest wall-to-wall distance. Then, the low intensity may reflect a low number of such inner-outer tube pairs in the sample.

6.1.2 5 % sample measurements: N₂- Doping effects

We can now compare easily the statements made from figure 6.1 with with figure 6.3 where the feedstock of the sample was N₂-doped (5 % Acetonitrile).

We clearly see that the influence of nitrogen only affect the spectra for low Raman shift frequency or big diameter tubes (among them cluster (12,10) and (11,9)), respectively. The Raman-shift limit can be drawn approximately at 190 cm^{-1} . All peaks above this limit are exactly at the same position along with the same resonance profile as in the spectra of the 0 % sample. Below this limit there are some significant changes of the resonance profiles observable. The most outstanding change is (as mentioned above) the disappearance of cluster (12,10) and (11,9). The other cluster do not seem to be affected in peak position or resonance profile by the nitrogen doping. The intensity ratios of the cluster resonances to the other broader peaks (above 190 cm^{-1}) stay very similar as well. There is one interesting difference, though: The split components of the respective clusters ((9,6) and (10,7)) now can be enveloped by a Gauss-like curve, just as cluster (12,10) and (11,9) in the 0% sample spectra.

Thus, figure 6.3 supports all presumptions made based on figure 6.1 and demonstrates that that N₂-doping has no influence on the growth of nanotubes with diameters below $\sim 1.2\text{ nm}$ (refers to $\sim 190\text{ cm}^{-1}$, depending on A,B in equation 2.11). Particularly, it has no influence on the growth of DWNTs, provided the diameter is small enough.

A closer look at the Raman-shift regions of cluster (12,10) ($\sim 150\text{-}180\text{ cm}^{-1}$) and (11,9) ($\sim 165\text{-}190\text{ cm}^{-1}$) of figure 6.3 reveals another interesting feature: The strong and narrow resonances are the *only* peaks which disappear in their corresponding regions. The

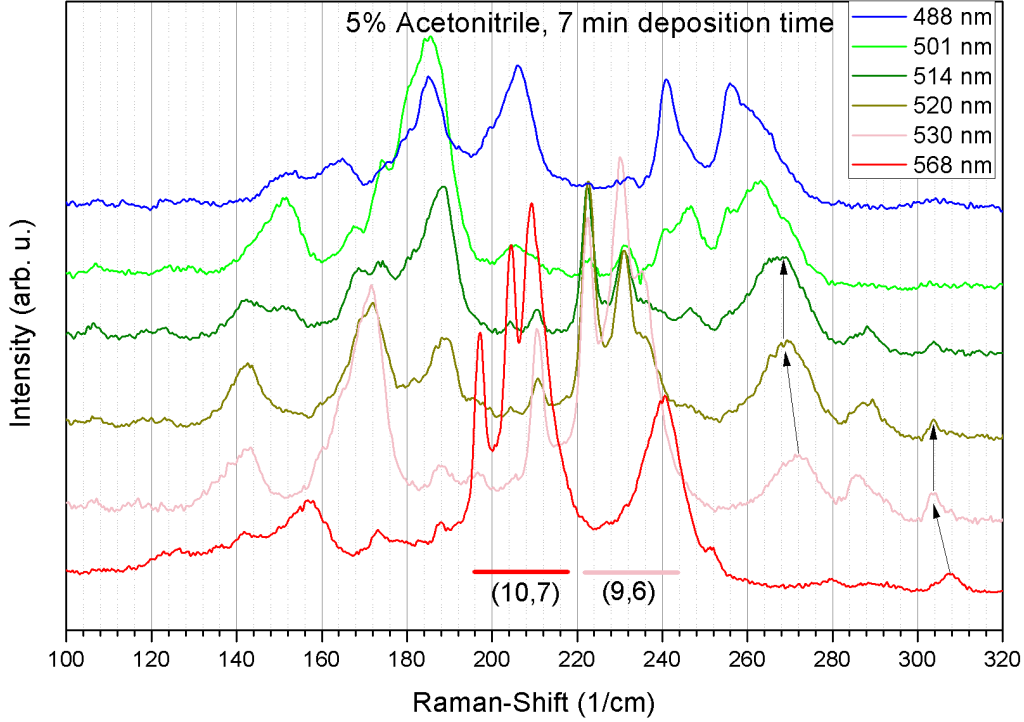


Figure 6.3: RBM peaks for different laser excitation energies for the 5 % acetonitrile sample. The RBM profile changes below $\sim 190 \text{ cm}^{-1}$ and two splitting cluster disappeared in this region. Apart from different intensity distributions, the all other features above that limit get confirmed.

broader, bundle-like peaks, which overlapped in figure 6.1 with the strong narrow peaks, are not affected by the nitrogen doping. This is in contrast to the broader peaks below 150 cm^{-1} , where the Raman-profiles are changed significantly. This aspect is another indication for DWCNTs, as the region below 150 cm^{-1} should contain the outer tube (or in-phase) resonances. Thus, if the growth of the outer tubes is prevented by the nitrogen doping, the growth of the inner tubes is prevented as well.

The overall intensity of the spectra from the 5% sample is quite a bit weaker than from the 0% sample, which can be seen by the increased signal noise. This change of intensity is strongly related to experimental influences and therefore not necessarily caused by a smaller number of nanotubes in the 5% sample. G-line measurements suggest a overall-intensity reduction by a factor of 0.5, which roughly matches the increase of the signal noise intensity.

Changes below 150 cm^{-1} through N_2 -doping

As this region contains the fitting tube diameters for outer tubes ($d > 1.7 \text{ nm}$), the significant modifications of the observed diameter distribution through nitrogen are of particular interest for the growth of DWCNTs. Summarising the are two major changes

for the inner tube resonance clusters observed through N₂-doping: First, cluster (12,10) and (11,9) vanish. Second, cluster (9,6) and (10,7) change slightly their appearance, as their split components form a different Raman profile shape. This means the higher the Raman shift of the corresponding split component, the larger is the intensity of it.

So we can ask an interesting question: Can the observed changes below 150 cm⁻¹ be related to one of these changes of the inner resonance clusters? It can, but these presumptions are rather speculative: At ~ 136 cm⁻¹ there is a quite strong peak (at 520, 514 nm) disappeared in the nitrogen doped sample, which could be assigned to a candidate for outer tubes of the cluster (10,7) inner-tube split components. The assignment of these potential outer tubes to (20,7) is not very secure (by using A=228, B=15 of bundles in equ. 2.11), as the influence of the bundling-interaction on the outer tubes (or in-phase) vibration energy cannot be easily assessed. Nevertheless, this assignment is supported by the analysis in the following section. This outer tube assignment would correspond to the intensity-loss of the split component of cluster (10,7) at 204 cm⁻¹.

Whether this tube assignment of the peak at 136 cm⁻¹ is correct or not, it is very plausible that the impact of Nitrogen on big-diameter tube growth has subsequent influence on the intensity-distribution of the split components of cluster (9,6) and (10,7) (see figures 6.1 and 6.3).

This presumption gets expressed by the fact that the split components assigned to larger interwall distances (lower Raman shift split components of the corresponding cluster) tend to exhibit larger intensities for the non-doped sample as for the nitrogen doped sample. Thus, a DWNT formation with large interwall distance would be less likely for the nitrogen doped sample, as the growth of large outer wall tubes might be more likely prevented.

A further investigation of the lower Raman -shift features requires lower excitation energies in order to bring the lower energy transitions in resonance (see fig. 2.4).

6.2 Discussion of inner tube resonances

6.2.1 Splitting cluster width

The range of the inner tube clusters have been significantly underestimated in this previous works (about 10 years ago), the typical range of the effect is presented correctly in more recent works (e.g. [45]). According to them, the width of the inner tube splitting cluster can easily exceed 20-30 cm⁻¹.

The fact that the splitting clusters presented here refer to bigger diameter tubes should not have significant influence on the cluster width (or the influence of the interwall interaction on the RBM mode, respectively): The increased mass of the inner tubes here should be compensated by the simultaneously increased inner-outer tube coupling constant per unit length (see equ. 2.7). Therefore the range of all observed inner tube splitting clusters (~ 20 cm⁻¹) is of ordinary magnitude, similar to peapod grown samples. However, this does not mean that this quantity is completely independent of the absolute inner/outer tube diameter, this is only a rough estimate. Previous simulations of inner-outer tube interactions suggest a slightly larger RBM blueshift at constant WtW distance

for big diameter DWNTs ([12]). The natural SWNT-RBM force constant in vacuum were obtained via atomistic force field calculations and the DWNT-coupling force constants via continuum model simulations.

The major influence on the cluster splitting width is the production process anyway. The distribution of inner-outer tube distance population is different for CVD-produced samples compared peapod grown ones, as here inner and outer tube grow (nearly) simultaneously. Therefore the growth conditions for the inner tubes are significantly different for CVD- grown specimen, which also results (in most cases) in a lower degree of perfection of the inner tube growth.

The better growth conditions for peapod inner tubes should also result in a different distribution of the inner-outer tube distance ΔR . This can be directly depicted from comparisons of CVD and peapod grown inner tube resonance cluster by comparing the intensity-distribution of the split components (e.g. [46]). This distribution is always shifted towards lower RBM frequencies for CVD-produced samples, which reflects that larger WtW-distances are preferred here. This fact is generated by a different growth mechanism in catalyst-based methods to produce DWNT, as mentioned previously.

The mapping of the observed clusters to one corresponding specific inner tube chirality strongly supports the assumption of relatively large ΔR for all clusters, as the RBM-frequency blueshift for all observed split components is rather low ($\Delta\omega \sim 0\text{-}15 \text{ cm}^{-1}$) compared to typical C_{60} peapod inner tube RBM clusters. The reference point of the redshift ($\Delta\omega=0$) was obtained by using the equation $\omega_{RBM} = 228/d$ for suspended high-quality SWNT [20].

6.2.2 Assignment to outer tubes

Although ΔR (and subsequently possible outer tube chiralities) are a priori not known, it may be possible to get an idea for these unknown quantities by using data of previously measured large diameter DWNT and obtaining an approximation for the function $\Delta\omega(\Delta R)$. This already has been done previously, but only for very small diameter inner tubes, e.g. ref. [32]. The results based on experimental data then can be compared with simulated data ([12, 51, 54]).

The shape of the VdW-interaction potential (and therefore $\Delta\omega(\Delta R)$) crucially depends on the curvature of the nanotubes and therefore their radii. For this reason, a fit of $\Delta\omega(\Delta R)$ is only valid for a very small region around a specific inner tube diameter.

The publication of Liu et al. ([19]) features a list large diameter CVD-grown DWNTs, whose inner-outer tube chiralities were rigorously determined through structural analysis (XRD) and mapped to their corresponding RBM peak positions. With this data a fit of the function $\Delta\omega(\Delta R)$ would be no problem. The diameters of these inner tubes are slightly larger ($d > 1.6 \text{ nm}$) than those investigated in this work. This should not lead to a significant error, as the difference is not that big and curvature changes should not have a large effect for big diameter inner tubes.

As performed previously, the approach $\Delta\omega(\Delta R) = (A/\Delta R)^B + C$ with the fitting parameters A, B, C should be used to get a proper dependence. Unfortunately, there is too little data for a good fit of this function, especially for large values of ΔR . This

makes a fit with these three parameters not practicable, as there are too much degrees of freedom. However, previous investigations deliver a rough boundary condition on the WtW distance where the influence on the RBM frequency vanishes ([28, 33]). This (upper) boundary can be set at $\Delta R_{0u} \sim 0.40$ nm. With this consideration a linear fit of $\Delta R(\Delta\omega)$ should at least give an lower boundary for ΔR_{0l} . A justification for this might be the relatively large values of ΔR in the used data sample, as only 2 values are at the 'ideal' distance of 0.34 nm all other values are significantly higher. Additionally it is assumed that the large-diameter DWNTs found and investigated in this work also have large values of ΔR , which should also justify the use of the derived fitting function. Thus, i consider only the first order after rearranging the equation given above to $\Delta R = \frac{A}{(\Delta\omega - C)^{1/B}}$. Higher order terms make no acceptable fit possible, as neither the inner nor the outer tube diameter is kept constant in our data sample.

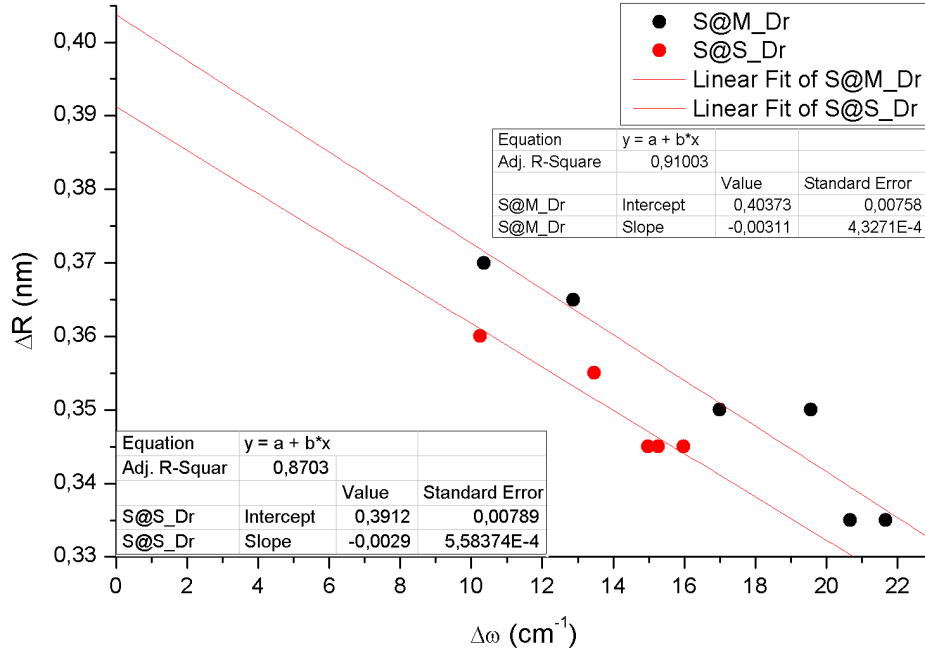


Figure 6.4: Linear fits of $\Delta R(\Delta\omega)$ using data of investigated large diameter CVD-grown DWNTs by Liu et al. ([19]). There is a clear offset between DWNTs with metallic and semiconducting outer tube visible. The separation between these configurations (S@M and S@S, respectively) clearly reduces the mean variation to the linear fit. Taking the statistical errors into account, this offset should not have a big impact on the outer tube diameter assignment. See the text for further discussion.

The plot of the experimental results of Liu et al. ([19]) in figure 6.4 reveals a small offset for DWNTs featuring a metallic outer tube (red points). All DWNTs represented in this figure have a semiconducting inner tube (hence only S@M and S@S inner-outer tube configurations). This is suggesting a small influence on the VdW-interaction by

π -electron polarisation effects. It has to be considered that these metallic outer-tubes have a very large diameter (2.3 - 3 nm), therefore many electrons can contribute to this behaviour. It should not be very influential for the mostly smaller diameter outer tubes on the quartz-samples studied in this work. Subsequently, only the fit based on S@S-DWNT configurations is used for the further assignment. Nevertheless, this could be the potential reason an individually wrong outer tube assignment.

The lower linear fit presented in figure 6.4 delivers a reasonable value for the lower boundary of $\Delta R_{0l} \sim 0.39 \pm 0.01$. With help of this function a mapping to possible outer tube families has been achieved. The results are presented in table 6.1.

The "helping function" for mapping to outer tube diameters derived this way should hopefully be able to give a good idea for the possible outer tube chiralities. Of course, there has to be boundary conditions considered: For the zero-blueshift WtW distance (the intercept) the linear approximation does not provide a good mapping to outer tubes (only lower boundary), therefore the corresponding outer tube has to have a larger diameter than assigned by the function. Similarly, the linear approximation should also get worse and worse for small WtW distances below ~ 0.35 nm. However, the approximation is hoped to work for WtW-distances between ~ 0.37 and 0.35 nm within a error tolerance of ± 0.01 nm (rounded up error from the fit). Indeed, with these considerations in mind a very plausible assignment to outer tube families is achieved for *all* 4 inner-tube resonance clusters (0 % sample).

Assuming the assignment to the corresponding outer tubes is correct, the zone-folding (DFT-corrected) outer tube diameters (and the WtW-distances) are subsequently known very accurately. With these iteratively corrected values, a good fit of the function $\Delta\omega(\Delta R) = (A/\Delta R)^B + C$ for every inner tube cluster should be possible. The only problem is the low number of observed split components. At least for cluster 2 and 4 there are 5 components for each cluster visible. A larger range of WtW distances would be required to perform meaningful fits. However, some conclusions can be drawn from the plots of the RBM-blueshift against ΔR .

Figure 6.5 and table 6.1 are based on an assignment, which is provided by the linear fit of the data by Liu et al. [19]. It should be pointed out that this assignment is not unique, there is a pool of several possible outer tube for one specific split component. This assignment prefers one outer-tube family ($2n+m=\text{const}$) per cluster, although the growth probability is independent of family-affiliation. Nevertheless, this assignment provides a good reproduction of the linear behaviour of the RBM-blueshift in dependence of large values of ΔR previously assumed.

The broad peak on the right (high RBM-blueshift/small WtW distances) side visible for every cluster, has been assigned to an additional split component of the corresponding cluster, although an assignment to nanotube bundles would be also possible sometimes. Therefore a modification of the inner tube transition energies for WtW-distances below ~ 0.34 nm in addition to the broadening (decreased phonon lifetime) of the RBM resonance is assumed. This assumption provides reasonable plots for the function $\Delta\omega_+^{\text{exp}}(\Delta R)$ (see figure 6.5). Figure 6.5 compares very well with similar simulated results in ref. [12].

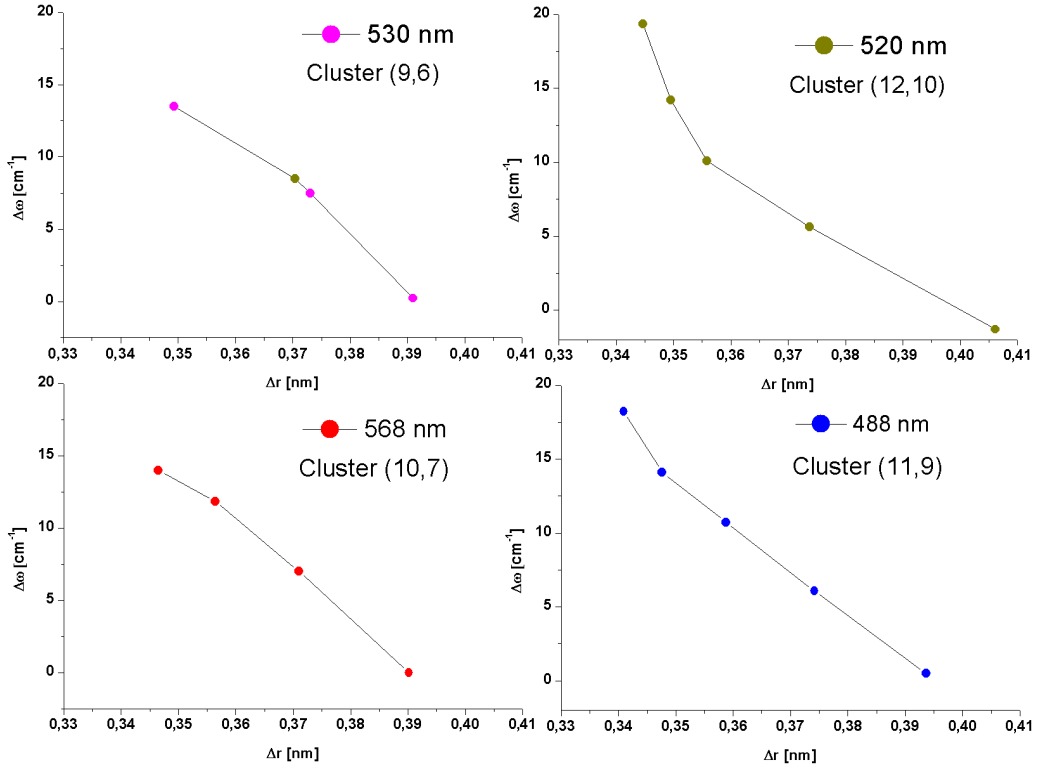


Figure 6.5: RBM blueshift is plotted against the corresponding WtW distance ΔR for each cluster after assigning each split component to a outer tube. This assignment provides a reasonable dependence of $\Delta\omega$ on ΔR . The two plots on the right side and the two plots on the left side, respectively, are very similar, which reflects the influence of the absolute inner/outer tube diameters.

6.2.3 Intensity and linewidth

The large intensity and the narrow linewidths of these specific few split components can reflect a high degree of defect absence ([46, 47]) through enhanced electron state and phonon lifetimes, respectively. On the other hand, the intensities depend on the number of nanotubes in resonance, of course. Even though the investigated sample contains a large number of tubes per unit area, the enhanced scattering rate (proportional to exciton lifetime) can be estimated qualitatively by considering the other RBM peaks within a certain laser excitation wavelength. From figure 6.1 it can be seen that the enhancement in intensity does vary from cluster to cluster. Of course, this does not surprise, as the intensity depends strongly on the difference between laser energy and the transition energy $E_L - E_{ii}$ (as well as on $E_L - (E_{ii} + E_{\text{phonon}})$). As the resonance profile of cluster (12,10) is very well visible, a reliable increase of intensity about a factor of 3 can be concluded (for 520 nm). For cluster (11,9) a similar factor is very plausible, as the transition energy is probably matched very good for 488 nm. Although this fact should also more or less true for cluster (10,7) and (9,6), the enhancement is reduced to a factor of ~ 2 for these smaller diameter inner tubes. This does not change for the nitrogen doped sample (where

Outer tube assignment for observed cluster split components				
$(m_o, n_o)_{2m+n}$	(m_i, n_i)	Δr [nm]	$\Delta\omega_+^{\text{exp}}$ [cm ⁻¹]	λ_L of max. visibility
(18,8) ₄₄	(9,6)	0.391	0	530 nm
(19,6) ₄₄		0.373	7.5	
(14,12) ₄₀		0.37	8.5	
(22,0) ₄₄		0.349	13.5	
(17,17) ₅₁	(12,10)	0.406	-1	520 nm
(18,15) ₅₁		0.374	5.6	
(21,11) ₅₃		0.356	10.08	
(20,12) ₅₂		0.35	14.22	
(19,13) ₅₁		0.345	19.37	
(19,9) ₄₇	(10,7)	0.39	0	568 nm
(20,7) ₄₇		0.371	7	
(21,5) ₄₇		0.356	11.85	
(22,3) ₄₇		0.347	13.85	
(21,10) ₅₂	(11,9)	0.394	0	488 nm
(22,8) ₅₂		0.374	6.08	
(23,6) ₅₂		0.359	10.718	
(24,4) ₅₂		0.348	14.1	
(25,2) ₅₂		0.341	18.23	

Table 6.1: This assignment to outer tubes to the observed split components corresponds to figure 6.5 and is based on the experimental data of Liu et al. ([19], see figure 6.4). The zero-shift position was determined by $\omega_0 = (228 \pm 1)/d$ (for suspended (absence of environmental perturbations) SWCNTs). Each cluster observed features an intense and narrow split component at this position (within the error limits).

cluster (12,10) and (11,9) disappeared). These factors for the enhancement in intensity do not apply for the broader peaks on the high RBM shift side of each cluster.

Especially for cluster (10,7) it should be pointed out that the inner (10,7) tubes are in resonance with the upper energy transition $E_{11}^u = 2.15$ eV of the two transitions through trigonal warping. The upper optical transitions are generally attributed with a significantly lower electron-phonon matrix element ([48]). This fits into the reduced intensity enhancement of this cluster, subsequently there is not necessarily a lower number of DWNT compared to cluster (12,10) and (11,9). The same holds for cluster (9,6), with the difference that quantum interference effects between the energy transition E_{11}^u and E_{11}^l may have to be considered here. This could be responsible for the apparent energy transition downshift of 50 meV mentioned previously.

Linewidth

In theory, the linewidth of an Raman mode is proportional the reciprocal phonon population lifetime ([14]). Unfortunately, the measured Raman spectra are significantly

broadened due a spectrometer response. Depending on the resolution-power of the Raman spectrometer, the photons get elastically scattered before they hit the detector. This results in a Gaussian share in the lineshape of the measured RBM peaks. Subsequently, Raman resonances exhibit a Voigtian lineshape, which is a convolution between a Lorentzian and a Gaussian function. The Lorentzian share is the natural line of the mode.

In order to quantify the phonon lifetime through the RBM linewidth, a significant reduction of the gaussian share has been achieved by using the high resolution mode of the DilorXY Raman spectrometer. Now the linewidth can be quite accurately be determined by performing a multiple peak fit with Lorentz curves. However, there is still a small Gaussian share present and the fitted linewidth has to be considered as an upper boundary for this reason. In order to reveal the pure Lorentzian part of the line, a Voigtian fit was performed of an intense Neon lamp line measured in HR mode. The obtained value for the Gaussian width was taken as a fixed parameter in the Voigt fit of the RBM-peak at 197 cm^{-1} .

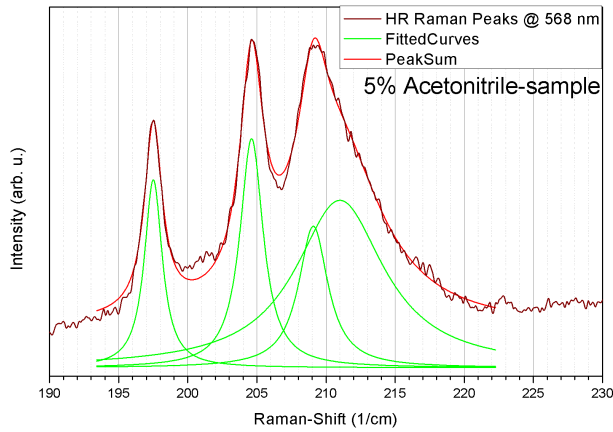


Figure 6.6: The high resolution measurement (568 nm) of the 5%-sample reveals linewidths from ~ 1.5 to 2.3 cm^{-1} (first three peaks starting from the left). The broad fourth peak at 211 cm^{-1} has a linewidth of $\sim 7\text{ cm}^{-1}$, which is a typical value for SWCNTs.

Figure 6.6 shows a rather good multiple curve fit by using Lorentz profile, but the (small) Gaussian part was ignored here. The left peak shows a FWHM of $\sim 1.5\text{ cm}^{-1}$ for the Lorentz fit, whereas the Voigtian fit with fixed parameter reveals a pure Lorentzian share of $\sim 1.3\text{ cm}^{-1}$. Thus, the reduction of 0.2 cm^{-1} can be applied for the other 3 peaks in figure 6.6.

The obtained results for γ_L are (from left to right) 1.3, 1.7, 2.3 and 7.6 cm^{-1} . Except for the broad peak at 211 cm^{-1} , these values are significantly lower (\sim factor 0.2) than for SWCNTs (bundled or in solution) typical ($7\text{-}10\text{ cm}^{-1}$). Therefore, the small FWHMs previously found for CVD inner tubes ($\sim 0.6\text{-}0.8\text{ cm}^{-1}$, [46, 33]) are not attained by a factor of ~ 2 .

It seems that the FWHM slightly increases for smaller WtW-distances (higher RBM-shift). The broad peak (which is assumed to be a split component, see discussion above) is at the highest Raman shift position for every cluster. If the assignment in table 6.1 is correct, this position corresponds to a WtW-distance of $\sim 0.34\text{ nm}$, which corresponds

generally to the optimal WtW distance ([28, 51], see figure 2.11).

This is suggesting an increase of environmental or defect perturbations for decreasing WtW-distances. Although the radial Lennard-Jones interaction potential should lead to a preference of ΔR around 0.34 nm, the growth-conditions of the corresponding chiralities seem to be significantly more perturbed compared to an ordinary inner tube growth in a "nanoclean" room from the outer tube.

The D/G-mode ratio allows to observe a significant decrease in defect concentration for increasing sample thickness. Especially for a laser excitation wavelength of 568 nm the D/G ratio is decreased by $\sim 50\%$ (figure 5.3). Additionally, the FWHM of the large G-mode peak (semiconducting LO branch) is clearly reduced.

However, this way no information about the broad inner tube resonances can be gained, as too many ordinary SWCNT in the sample contribute to the D-line. Nevertheless, it seems plausible that the broader lineshape of these peaks stem from defects.

6.2.4 Growth process

A comparative look at the analogous spectra of the thinner samples may give a good idea of the growth process of these splitting clusters (figure 6.7). It can be seen here that the broad resonances are much better visible than the other (not yet narrow) resonances, which reflects an earlier formation of a larger number of the corresponding smaller-diameter inner tubes. Thus, this observation goes hand-in hand with the preferred WtW-distance of 0.34 nm for inner-tube growth processes.

WtW distances and reaction time

This early visibility of the broad (or high shift-) resonances is an additional indication that the assignment of table 6.1, or at least the assignment to the WtW-distances ΔR (figure 6.4) is in principle correct. As mentioned previously, this peak cannot be assigned via zone-folding energy transitions and eqn. 2.11 with nanotube bundle parameters.

The fact that there is an indisposition of inner-outer tube pairs with smaller ΔR -values (compared to C_{60} -precursor DWNTs) is a well known feature of catalyst CVD-grown DWNTs (similar to $FeCp_2$ -precursor grown ones). The still quite large values for ΔR (minimum is 0.34 nm) may be related to suboptimal growth conditions (temperature, pressure) for CVD-DWNTs. The more perturbed environment together with the simultaneous growth of inner and outer tube may result in a higher probability for a formation with larger deviation from the optimal ΔR .

DWNT growth rate and reaction time

The generally large diameters of the DWNTs may be explained by a lumping of the metallic catalyst particles with proceeding reaction time in the vacuum chamber. The DWNT formation is clearly not among the dominating growth-processes at early stages, as the cluster components only feature a barely or no visible intensity. This seems to change for increasing deposition time, where the growth rate explodes somewhere between 3 and 7 minutes. Beside the lumping of cluster particles, increasing pressure in

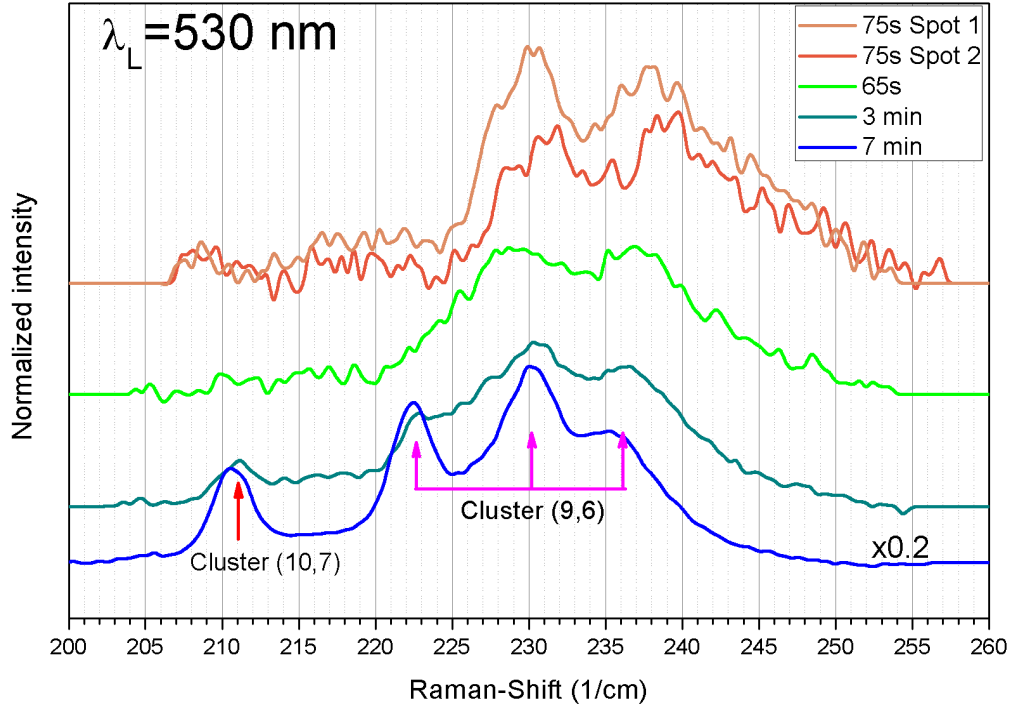


Figure 6.7: The growth of cluster (9,6) plus 1 peak of Cluster (10,7) (as indicated by arrows) with increasing sample thickness (from top to bottom) is shown here for 530 nm (2.33 eV) laser-excitation wavelength. All peaks are normalized with the intensity of their corresponding G-mode peak (LO). Therefore, also the clear enhancement in intensity for the thick sample (7 min deposition time, 5% acetonitrile) is demonstrated again (was scaled with factor 0.2). The split components at 211 and 222 cm^{-1} are not visible for the thinner samples, whereas the two at 230 and 236 cm^{-1} are always visible. The thinnest sample features a blueshift of 1-2 cm^{-1} for the latter peak.

the reaction chamber along with deposition time may also have impact on the DWNT growth rate.

Electronic energy transition modifications

An interesting feature of figure 6.6 is the left peak (at 210 cm^{-1} , which belongs to cluster (10,7) (see table 6.1). Contradicting the previous discussion, this peak is not broad and visible for lower film thickness. A membership to cluster (9,6) is impossible, due to the resonance profile (see figures 6.1, 6.3) and zone-folding transition energies (e.g. [7]). This indicates an increase of high quality inner tubes (narrow FWHM) for increasing sample thickness also for these specific small WtW-distance ($\Delta R \sim 0.34$ nm) inner-outer pairs ((10,7)@(24,0) according to table 6.1). The presence of this narrow split component at higher excitation energies also suggests that the high-quality of this inner tube comes along with an increase of the corresponding energy transition E_{11}^{upper} of about $\Delta E \sim 100$ meV.

This feature may not only be visible for cluster (10,7), but also for cluster (9,6) (same energy transition and already mentioned in section 6.1.1): As observable in figures 6.2, 6.1, 6.3, there are split components at 230 and 236 cm^{-1} for cluster (9,6) at a laser wavelength of 530 nm. At lower wavelengths (520 to 488 nm) there is a weak peak at $\sim 231 \text{ cm}^{-1}$ clearly visible for both figures 6.1 and 6.3. Thus, for these wavelengths there is without doubt (with help of accurate post-measurement calibration) an additional distinct split component visible. However, it can not be directly seen whether it is a narrow resonance due to its weakness. The visibility up to 488 nm strongly suggests an blueshift in transition energy similar to the one observes in figure 6.7. The change in ω_{RBM} (not visible in figure 6.7) of $\sim 1 \text{ cm}^{-1}$ may show a change in outer-tube diameter (as well as chirality, see table 6.1). This again suggests that a growth of a corresponding (maybe high quality) inner tube at WtW-distances around 0.34 nm goes along with a change in energy transition.

The broad resonances on the high Raman-shift side of the other clusters (see figure 6.1) suggest a decrease of their corresponding transition energies. A modification of the energy transitions by Lennard-Jones interaction (for most transition a decrease) has been investigated previously for bundles and DWNTs (ref. [8, 47, 25]).

A modification of the growth conditions may prevent or cause the formation of specific inner-outer tube pairs or improve the quality of larger diameter inner tubes (smaller ΔR). A longer depositions time increased the visibility of the inner tube resonance clusters.

Peak positions - RBM shifts

Figure 6.7 also features an influence on the peak position of the inner tube resonances. The broad resonance on the high shift side is clearly blueshifted 1 - 2 cm^{-1} for the thinnest sample (75s deposition time). This blueshift is reliably confirmed by an additional spectra taken at a different illuminated sample spot (beige line) and accurate post-measurement calibration. This seems strange if the RBM mode is viewed as an individually oscillating tube, as the inner tubes should be protected from the environment by the outer tubes. This should prevent any influence on the RBM peak position.

This effect is already discussed in chapter 5.1, now this has to be applied to the outer tubes. They are exposed to more tube bundling for the thin samples than for the thicker samples. This external pressure may result in a slight reduction of the outer tube diameter and/or a stiffening of the outer tube force constant. As described in section 2.4.1, this also may affect the vibrational energy of the collective counter-phase mode. The observed shift matches very well with the continuum model calculations of DWNT bundles in ref [12] for WtW-distances $\sim 0.34 \text{ nm}$.

Such an influence on inner tube resonance positions is neither expected nor observed for larger WtW-distances. A growing distance results in a weaker coupling of the inner and outer tube until the collective counter-phase oscillation mode gets very insensitive against external perturbations. In this context, if the coupling gets very weak the oscillation is probably better described as individually oscillating tubes.

6.3 Summary of chapter 6

The RBM-Raman spectra of the nanotubes deposited on the substrate by CCVD show clearly the formation of typical inner tube splitting clusters of DWNTs. The relative quantity of the DWNT depends strongly on the layer thickness of carbon material on the quartz substrate. Four different inner tube clusters could be observed for laser excitation energies from 2.18 to 2.54 eV (figure 6.1) for the thick sample (7 minute deposition time) without N₂-doping. The corresponding N-doped sample shows similar results (figure 6.3), with the exception the two clusters of the larger diameter inner tubes (>1.3 nm) (almost) vanish.

With help of previous investigations of large diameter CVD grown DWNTs, an assignment for each split component to a specific inner-outer tube pair chirality has been achieved. This assignment suggests relatively large WtW-distances up to 0.39-0.4 nm. According to continuum model calculations ([51, 28, 12]), the coupling constant owing to tube-tube interaction effectively vanish for these values for ΔR . Subsequently, no blue-shift in RBM-frequency is observed for the corresponding inner-outer tube split components.

Of course, the interaction-free split components always feature the lowest intensity, as the formation of such DWNTs occurs with lower probability. Hence, the formation-preference of DWNTs featuring values of ΔR around the optimal WtW-distance (0.34 nm) is observed.

The observed high intensities of the clusters reflect an enhanced electron-phonon coupling (excited state lifetime) as well as an increasing quantity of DWNTs for increasing carbon layer thickness. The reduction of the D/G-mode ratio for increasing thickness suggests an relative increase of the high quality-inner tube share compared to the other nanotube material. The large diameter DWNT-growth may be related to changing growth conditions with increasing deposition time in the vacuum chamber. On the one hand the metallic catalyst particles may lump together, on the other hand the pressure is increasing with increasing growth time. Both effects may favour the growth of larger nanostructures and subsequently larger diameter SWNTs and/or DWNTs at higher positioned carbon film layers.

The FWHM strong and narrow RBM split components are observed to be slightly increasing. The split components with the highest RBM-blueshift (observed for all clusters) features a very broad SWCNT-like linewidth, whereas the interaction-free split components with no blueshift feature the highest quality inner tubes with a deconvoluted Lorentzian linewidth down to 1.3 cm⁻¹. Thus, the observed narrowness of the lines do not reach the level of those of previously grown CVD-DWNT by a factor of ~ 2 (this applies for cluster (10,7), similar values for the others can be expected from the NR spectra). Nevertheless, the quality of the inner tubes seems to be significantly better than ordinary SWCNTs ($\gamma \sim 7.8$ cm⁻¹).

It should be noted that the resonance profile for the broad resonances differ slightly from the strong and narrow split components. This indicates an influence of the close (0.34 nm) WtW-distance on the energy transitions. An example of a blueshift of the E_{11}^{upper} -transition is shown in figure 6.7. The broad resonances are already very well

visible for the thinner samples, which underlines the preference of these inner tubes to grow at WtW distances of 0.34 nm.

For the broad resonances potentially corresponding to small WtW-distance inner-outer tube pairs, an influence of the outer tube on the vibrational properties of the inner tubes (or collective counter-phase mode) can be observed in fig. 6.7. Similar to various SWNT peaks presented in previous chapters (e.g. fig. 5.1), slightly higher RBM-peak positions for thinner samples can be observed. This is explained by a denser tube array arrangement for thin samples compared to thicker samples. The influence on the inner tube may be explained by a slight modification of the WtW-distance and/or force constant of the collective counter-phase oscillation through a different influence on the outer tubes through tube bundling.

7 Conclusions and future perspectives

Small Raman shift sensible physical effects can deliver useful information about the properties of nanoscale structures, including carbon nanotubes. It is important to be aware of the accuracy of the Raman scale in order to avoid systematic errors. With an effortless calibration method Raman spectroscopy is a simple and very powerful tool for quantifying sensible atomistic properties. As for the measurements carried out for this work, there is no special sample preparation needed. As-grown nanotube arrays were measured by focusing the laser beam onto the carbon film of quartz plate at room temperature. Despite the simple experimental setup, a consisted analysis of low (bundles) and high (DWNTs) interaction affects has been achieved. This simple application on nanomaterials offers a lot of possibilities for effortless and precise characterization, providing a good theoretical understanding of the electronic and vibrational properties of the material. On the other hand, a precise Raman spectrum (in position and intensity) can enhance the progress theoretical understanding of these properties.

Collective DWNT oscillations are a prominent example for high pressure effects. The interaction potential between inner and outer tubes is not fully understood for different DWNT-configurations. A precise Raman scale is a prerequisite for the experimental investigation of such potentials via Raman spectroscopy. A correct interpretation of the vibrational nature also may help to gain information about the environmental properties around and inside of DWNTs and defects related to them.

In context with this work, DWNT vibration split components have been observed which can be well quantified assuming individually oscillating nanotubes rather than collective oscillations of inner and outer tubes. A better interpretation of the observed resonances may facilitate the understanding emerging properties of van der Waals-coupled superstructures, such as multilayer of graphene and superlattice of nanoparticles.

Bibliography

- [1] E. Antunes, A. Lobo, E. Corat, V. Trava-Airoldi, A. Martin, and C. Verissimo. Comparative study of first- and second-order Raman spectra of MWCNT at visible and infrared laser excitation. *Carbon*, 44(11):2202–2211, Sept. 2006.
- [2] P. T. Araujo, S. K. Doorn, S. Kilina, S. Tretiak, E. Einarsson, S. Maruyama, H. Chacham, M. A. Pimenta, and A. Jorio. Third and Fourth Optical Transitions in Semiconducting Carbon Nanotubes. 067401(February):1–4, 2007.
- [3] P. Ayala, R. Arenal, A. Loiseau, A. Rubio, and T. Pichler. The physical and chemical properties of heteronanotubes. *Reviews of Modern Physics*, 82(2):1843–1885, June 2010.
- [4] P. Ayala, R. Arenal, M. Rümmeli, a. Rubio, and T. Pichler. The doping of carbon nanotubes with nitrogen and their potential applications. *Carbon*, 48(3):575–586, Mar. 2010.
- [5] S. Berciaud, S. Ryu, L. E. Brus, and T. F. Heinz. Probing the intrinsic properties of exfoliated graphene: Raman spectroscopy of free-standing monolayers. *Nano letters*, 9(1):346–52, Jan. 2009.
- [6] E. Cigeroglu and H. Samandari. Nonlinear free vibration of double walled carbon nanotubes by using describing function method with multiple trial functions. *Physica E: Low-dimensional Systems and Nanostructures*, 46:160–173, Sept. 2012.
- [7] M. Dresselhaus, G. Dresselhaus, R. Saito, and a. Jorio. Raman spectroscopy of carbon nanotubes. *Physics Reports*, 409(2):47–99, Mar. 2005.
- [8] C. Fantini, a. Jorio, M. Souza, M. Strano, M. Dresselhaus, and M. Pimenta. Optical Transition Energies for Carbon Nanotubes from Resonant Raman Spectroscopy: Environment and Temperature Effects. *Physical Review Letters*, 93(14):147406, Sept. 2004.
- [9] G. Gouadec and P. Colomban. Raman Spectroscopy of nanomaterials: How spectra relate to disorder, particle size and mechanical properties. *Progress in Crystal Growth and Characterization of Materials*, 53(1):1–56, Mar. 2007.
- [10] A. A. Green and M. C. Hersam. double-wall carbon nanotubes. 4(December 2008), 2009.

- [11] A. Grüneis, M. Rümmeli, C. Kramberger, A. Barreiro, T. Pichler, R. Pfeiffer, H. Kuzmany, T. Gemming, and B. Büchner. High quality double wall carbon nanotubes with a defined diameter distribution by chemical vapor deposition from alcohol. *Carbon*, 44(15):3177–3182, Dec. 2006.
- [12] S.-p. Han and W. a. Goddard. Coupling of Raman radial breathing modes in double-wall carbon nanotubes and bundles of nanotubes. *The journal of physical chemistry. B*, 113(20):7199–204, May 2009.
- [13] A. Jorio. Raman Spectroscopy in Graphene-Based Systems: Prototypes for Nanoscience and Nanometrology. *ISRN Nanotechnology*, 2012(2):1–16, 2012.
- [14] K. Kang, T. Ozel, D. G. Cahill, and M. Shimt. Optical phonon lifetimes in single-walled carbon nanotubes by time-resolved Raman scattering. *Nano letters*, 8(12):4642–7, Dec. 2008.
- [15] C. Kramberger, R. Pfeiffer, H. Kuzmany, V. Zólyomi, and J. Kürti. Assignment of chiral vectors in carbon nanotubes. *Physical Review B*, 68(23):235404, Dec. 2003.
- [16] J. Kürti, G. Kresse, and H. Kuzmany. First-principles calculations of the radial breathing mode of single-wall carbon nanotubes. 58(14):8869–8872, 1998.
- [17] H. Kuzmany, W. Plank, R. Pfeiffer, and F. Simon. Raman scattering from double-walled carbon nanotubes. (September 2007):134–140, 2008.
- [18] B. Liu, B. Yu, and M. Zhang. Catalytic CVD synthesis of double-walled carbon nanotubes with a narrow distribution of diameters over Fe–Co/MgO catalyst. *Chemical Physics Letters*, 407(1-3):232–235, May 2005.
- [19] K. Liu, X. Hong, M. Wu, F. Xiao, W. Wang, X. Bai, J. W. Ager, S. Aloni, A. Zettl, E. Wang, and F. Wang. Quantum-coupled radial-breathing oscillations in double-walled carbon nanotubes. *Nature communications*, 4:1375, Jan. 2013.
- [20] K. Liu, W. Wang, M. Wu, F. Xiao, X. Hong, S. Aloni, X. Bai, E. Wang, and F. Wang. Intrinsic radial breathing oscillation in suspended single-walled carbon nanotubes. *Physical Review B*, 83(11):113404, Mar. 2011.
- [21] I. O. Maciel, N. Anderson, M. A. Pimenta, A. Hartschuh, H. Qian, M. Terrones, H. Terrones, J. Campos-Delgado, A. M. Rao, L. Novotny, and A. Jorio. Electron and phonon renormalization near charged defects in carbon nanotubes. *Nature Materials*, 7:878–883, 2008.
- [22] G. Mahan. Oscillations of a thin hollow cylinder: Carbon nanotubes. *Physical Review B*, 65(23):235402, May 2002.
- [23] J. Maultzsch, S. Reich, and P. Ordejón. Vibrational properties of double-walled carbon nanotubes. *AIP CONFERENCE . . .*, pages 8–11, 2003.

- [24] T. Natsuki, G. J. H. Melvin, and Q.-Q. Ni. Vibrational Frequencies and Raman Radial Breathing Modes of Multi-Walled Carbon Nanotubes Based on Continuum Mechanics. *Journal of Materials Science Research*, 2(4):1–11, July 2013.
- [25] M. O’Connell, S. Sivaram, and S. Doorn. Near-infrared resonance Raman excitation profile studies of single-walled carbon nanotube intertube interactions: A direct comparison of bundled and individually dispersed HiPco nanotubes. *Physical Review B*, 69(23):235415, June 2004.
- [26] M. H. Park, J. W. Jang, C. E. Lee, and C. J. Lee. Interwall support in double-walled carbon nanotubes studied by scanning tunneling microscopy. *Applied Physics Letters*, 86(2):023110, 2005.
- [27] F. V. Pdiez. Raman Spectroscopy of Double Walled Carbon Nanotubes with Different Metallic and Semiconducting Configurations by LIBRARIES AfcNiVES. 2010.
- [28] R. Pfeiffer, C. Kramberger, F. Simon, H. Kuzmany, V. N. Popov, and H. Kataura. Interaction between concentric tubes in DWCNTs. *The European Physical Journal B*, 42(3):345–350, Dec. 2004.
- [29] R. Pfeiffer, H. Kuzmany, C. Kramberger, C. Schaman, T. Pichler, H. Kataura, Y. Achiba, J. Kürti, and V. Zólyomi. Unusual High Degree of Unperturbed Environment in the Interior of Single-Wall Carbon Nanotubes. *Physical Review Letters*, 90(22):225501, June 2003.
- [30] R. Pfeiffer, H. Kuzmany, F. Simon, S. Bokova, and E. Obraztsova. Resonance Raman scattering from phonon overtones in double-wall carbon nanotubes. *Physical Review B*, 71(15):155409, Apr. 2005.
- [31] R. Pfeiffer, H. Peterlik, H. Kuzmany, H. Shiozawa, a. Grüneis, T. Pichler, and H. Kataura. Growth mechanisms of inner-shell tubes in double-wall carbon nanotubes. *Physica Status Solidi (B)*, 244(11):4097–4101, Nov. 2007.
- [32] R. Pfeiffer, H. Peterlik, H. Kuzmany, F. Simon, K. Pressl, P. Knoll, M. H. Rummeli, H. Shiozawa, H. Muramatsu, Y. a. Kim, T. Hayashi, and M. Endo. A detailed comparison of CVD grown and precursor based DWCNTs. *Physica Status Solidi (B)*, 245(10):1943–1946, Oct. 2008.
- [33] R. Pfeiffer, T. Pichler, Y. Kim, and H. Kuzmany. Double-Wall Carbon Nanotubes. *Carbon Nanotubes*, 111:495–530, 2008.
- [34] R. Pfeiffer, F. Simon, H. Kuzmany, V. N. Popov, V. Zólyomi, and J. Kürti. Tube–tube interaction in double-wall carbon nanotubes. *Physica Status Solidi (B)*, 243(13):3268–3272, Nov. 2006.
- [35] V. Popov and L. Henrard. Breathinglike phonon modes of multiwalled carbon nanotubes. *Physical Review B*, 65(23):235415, May 2002.

- [36] V. Popov, V. Van Doren, and M. Balkanski. Lattice dynamics of single-walled carbon nanotubes. *Physical Review B*, 59(13):8355–8358, Apr. 1999.
- [37] P. M. Rafailov and A. R. Gon. Intermolecular Interaction in Carbon Nanotube Ropes. 435:435–442, 1999.
- [38] A. M. Rao, J. Chen, E. Richter, U. Schlecht, P. C. Eklund, R. C. Haddon, U. D. Venkateswaran, Y. K. Kwon, and D. Tománek. Effect of van der Waals interactions on the Raman modes in single walled carbon nanotubes. *Physical review letters*, 86:3895–3898, 2001.
- [39] H. Rauf, T. Pichler, R. Pfeiffer, F. Simon, H. Kuzmany, and V. Popov. Detailed analysis of the Raman response of n-doped double-wall carbon nanotubes. *Physical Review B*, 74(23):235419, Dec. 2006.
- [40] R. Saito, G. Dresselhaus, and M. Dresselhaus. Trigonal warping effect of carbon nanotubes. *Physical Review B*, 61(4):2981–2990, Jan. 2000.
- [41] G. G. Samsonidze, a. R. Saito, D. a. Jorio, E. M. a. Pimenta, E. a. G. Souza Filho, F. a. Grüneis, D. G. Dresselhaus, and M. S. Dresselhaus. The Concept of Cutting Lines in Carbon Nanotube Science. *Journal of Nanoscience and Nanotechnology*, 3(6):431–458, Dec. 2003.
- [42] H. Shiozawa, T. Pichler, A. Grüneis, R. Pfeiffer, H. Kuzmany, Z. Liu, K. Suenaga, and H. Kataura. A Catalytic Reaction Inside a Single-Walled Carbon Nanotube. *Advanced Materials*, 20(8):1443–1449, Apr. 2008.
- [43] F. Simon. Raman scattering of carbon nanotubes. Technical report, Universität Wien, 2005.
- [44] F. Simon. Electronic structure and vibrational properties of pristine and isotope engineered carbon nanostructures Ferenc Simon. 2006.
- [45] F. Simon, C. Kramberger, H. Peterlik, R. Pfeiffer, K. De Blauwe, T. Pichler, H. Kuzmany, K. Yanagi, Y. Miyata, and H. Kataura. Raman response from double-wall carbon nanotubes based on metallicity selected host SWCNTs. *Physica Status Solidi (B)*, 247(11-12):2880–2883, Dec. 2010.
- [46] F. Simon, A. Kukovecz, Z. Kónya, R. Pfeiffer, and H. Kuzmany. Highly perfect inner tubes in CVD grown double-wall carbon nanotubes. *Chemical Physics Letters*, 413(4-6):506–511, Sept. 2005.
- [47] F. Simon, R. Pfeiffer, and H. Kuzmany. Universal temperature dependence of optical excitation life-time and band-gap in chirality assigned semiconducting single-wall carbon nanotubes. *Physical Review B*, 2006.
- [48] H. Son, A. Reina, G. Samsonidze, R. Saito, A. Jorio, M. Dresselhaus, and J. Kong. Raman characterization of electronic transition energies of metallic single-wall carbon nanotubes. *Physical Review B*, 74(7):073406, Aug. 2006.

- [49] D. Song, F. Wang, G. Dukovic, M. Zheng, E. Semke, L. Brus, and T. Heinz. Direct Measurement of the Lifetime of Optical Phonons in Single-Walled Carbon Nanotubes. *Physical Review Letters*, 100(22):225503, June 2008.
- [50] T. Thurakitseree, C. Kramberger, P. Zhao, S. Aikawa, S. Harish, S. Chiashi, E. Einarsson, and S. Maruyama. Diameter-controlled and nitrogen-doped vertically aligned single-walled carbon nanotubes. *Carbon*, 50(7):2635–2640, 2012.
- [51] D. Vardanega, F. Picaud, and C. Girardet. Chiral interaction in double-wall carbon nanotubes: simple rules deduced from a large sampling of tubes. *The Journal of chemical physics*, 132(12):124704, Mar. 2010.
- [52] U. Venkateswaran, a. Rao, E. Richter, M. Menon, a. Rinzler, R. Smalley, and P. Eklund. Probing the single-wall carbon nanotube bundle: Raman scattering under high pressure. *Physical Review B*, 59(16):10928–10934, Apr. 1999.
- [53] J. Wei, B. Jiang, X. Zhang, H. Zhu, and D. Wu. Raman study on double-walled carbon nanotubes. *Chemical Physics Letters*, 376(5-6):753–757, July 2003.
- [54] G. Wu, J. Zhou, and J. Dong. Radial-breathing-like phonon modes of double-walled carbon nanotubes. (5), 2013.
- [55] Z. Wu, Z. Chen, X. Du, J. M. Logan, J. Sippel, M. Nikolou, K. Kamaras, J. R. Reynolds, D. B. Tanner, A. F. Hebard, and A. G. Rinzler. Transparent, conductive carbon nanotube films. *Science (New York, N. Y.)*, 305(5688):1273–6, Aug. 2004.
- [56] R. Xiang, Z. Zhang, K. Ogura, J. Okawa, E. Einarsson, Y. Miyauchi, J. Shiomi, and S. Maruyama. Vertically Aligned 13 C Single-Walled Carbon Nanotubes Synthesized by No-Flow Alcohol Chemical Vapor Deposition and their Root Growth Mechanism. *Japanese Journal of Applied Physics*, 47(4):1971–1974, Apr. 2008.

Danksagungen

An dieser Stelle möchte ich mich herzlich bei allen bedanken, die bei der Anfertigung dieser Arbeit zur Seite gestanden sind.

Ich möchte mich bei meinem Betreuer Prof. Thomas Pichler für die Anregungen und für die Möglichkeit bedanken, diese Arbeit im Rahmen seiner Gruppe zu erstellen.

Großer Dank gebührt auch Herrn Dr. Christian Kramberger für die zahlreichen hilfreichen Vorschläge, für die schnelle Korrespondenz und dafür, dass er mir bei allen Problemen stets zur Seite stand.

Des weiteren danke ich Lei Shi und vielen weiteren Gruppenmitgliedern für ihre Hilfsbereitschaft und für den unkomplizierten Zugang zu den benötigten Gerätschaften.

Ganz besonders Bedanken möchte ich mich bei meiner Familie und bei all den Menschen, die mich während des Studiums begleitet und unterstützt haben.

Lebenslauf

Gerald Pühringer

Geboren am 03. Juni 1987 in Linz, Oberösterreich

Schulische Ausbildung

September 1994 - Juni 1998: Volksschule VS 14, Linz

September 1998 - Juni 2006: Khevenhüller Gymnasium, Linz

Universitäre Ausbildung

Oktober 2007 - Juni 2011: Bachelorstudium Physik, Universität Wien

Oktober 2011 - Oktober 2014: Masterstudium Physik, Universität Wien

Zivildienst Oktober 2006 - Juni 2007: Rettungsdienst, Rotes Kreuz Linz